11-1-2020

Analogy Between Thermodynamic Phase Transitions and Creeping Flows in Rectangular Cavities

Miron Kaufman
Cleveland State University, m.kaufman@csuohio.edu

Petru S. Fodor
Cleveland State University, p.fodor@csuohio.edu

A NEW RESEARCH APPROACH FOR OBSERVING AND CHARACTERIZING LAND–ATMOSPHERE FEEDBACK

Volker Wulfmeyer, David D. Turner, B. Baker, R. Banta, A. Behrendt, T. Bonin, W. A. Brewer, M. Buban, A. Choukulkar, E. Dumas, R. M. Hardesty, T. Heus, J. Ingwersen, D. Lange, T. R. Lee, S. Metzendorf, S. K. Muppa, T. Meyers, R. Newsom, M. Osman, S. Raasch, J. Santanello, C. Senff, F. Späth, T. Wagner, and T. Weckwerth

A novel synergy of scanning lidar systems as well as other in situ and remote sensing instruments provides accurate 3D measurements of numerous dynamical and thermodynamical quantities to evaluate and improve our understanding of land–atmosphere interactions.

The L–A system includes the soil, the land cover such as vegetation, and the overlying atmosphere (see the appendix for a list of key acronyms used in this paper). The interaction of variables (e.g., related to the water and energy budgets) results in characteristic natural variabilities and regimes as well as their changes due to anthropogenic influences. The PBL is part of the L–A system and represents the interface between the land surface and the free troposphere. Through an exchange of momentum, energy, and water, the dynamics, the thermodynamic structure, and the evolution of the PBL affect the formation of shallow and deep clouds, convection initiation, and thus precipitation (Sherwood et al. 2010; Behrendt et al. 2011; Santanello et al. 2011; Van den Hurk et al. 2011; Wulfmeyer et al. 2015a). One of the most complex feedback loops is between soil moisture and precipitation (Seneviratne et al. 2010; Guillod et al. 2015; Santanello et al. 2018). Precipitation can be influenced directly by the surface fluxes (Ek and Holtslag 2004) and indirectly via PBL dynamics and mesoscale circulations (Taylor et al. 2012).

The PBL state and its evolution are strongly influenced by nonlinear feedbacks in the L–A system. These are due to two-way interactions between radiation, soil, vegetation, and atmospheric variables, which result in the diurnal cycles of surface fluxes. The feedbacks are relevant from local to global scales (Mahmood et al. 2014; Stéfanon et al. 2014), and their strength varies both regionally and seasonally in dependence of soil moisture, advection, and climate regimes. In locations where these feedbacks play an important role, it is likely that they will become even more important due to anthropogenic climate change (Dirmeyer et al. 2012). Thus, to improve our understanding of the state and the evolution of the L–A system as well as the dynamics and thermodynamics of the PBL, it is critical that feedbacks and fluxes between the different components, including entrainment at the top of the PBL, are well characterized and appropriately represented in weather, climate, and Earth system models (e.g., Seneviratne et al. 2010; Prein et al. 2015).

However, currently the representation of L–A feedbacks in models is far from sufficient. Errors

Publisher's Note: On 6 September 2018 this article was modified to correct reference and citation errors.

are clearly visible in simulated diurnal cycles of soil, surface, and PBL variables in forecast models (e.g., Shin and Hong 2011; Liu et al. 2011; Santanello et al. 2013; Milovac et al. 2016; Massey et al. 2016; Dirmeyer and Halder 2017) as well as in the propagation of these errors to the simulation of clouds and precipitation (e.g., Gentine et al. 2013; Tawfik et al. 2015). Climate models must be able to reproduce the range of L–A feedbacks including their effect on extreme events (Lenderink and Van Meijgaard 2008; Zolina et al. 2013) in order to project these into the future. This level of model performance has not yet been achieved (Warrach-Sagi et al. 2013; Vautard et al. 2013; Kotlarski et al. 2014; Lorenz et al. 2016).

Model horizontal grid increments continue to improve and approach the so-called gray zone of turbulence with resolutions between ~100 m and ~2 km (e.g., Honnert et al. 2011) where turbulence is neither unidirectional nor isotropic and thus not fully resolved (Wyngaard 2004; Honnert et al. 2016). It is currently unclear how to represent and parameterize turbulent variables and fluxes at these scales. Generally, the existing parameterization schemes were developed for coarser numerical models over essentially flat terrain. Therefore, the turbulence parameterization schemes need to be readjusted or even new scalable ones formulated in order to bridge the existing gap between mesoscale and LES scales (e.g., Baklanov et al. 2011; Honnert et al. 2011, 2016). Adaptations to the gray zones have been made by various groups (e.g., Boutle et al. 2014; Ito et al. 2015; Shin and Hong 2015; Honnert et al. 2016), but such approaches are strongly related to the selected PBL and surface-layer schemes. Therefore, over the entire range of model scales from tens of meters to tens of kilometers, it is necessary to study the representation of L–A interactions. Otherwise, improvements in the representation of clouds and precipitation can hardly be expected.

A key component in L–A feedbacks and their simulation is the turbulent mixing of momentum, heat, and moisture between the land surface to the top of the CBL. In the atmospheric surface layer, turbulent mixing is approximated by MOST. However, MOST assumes that the surface is homogeneous and that the fluxes are stationary, and then relates the fluxes only to surface-layer properties, which in turn depend on radiation, the soil and vegetation properties, and the properties of the air that interacts with the surface (e.g., Van de Boer et al. 2014). It is currently not understood how to modify MOST in terrain with heterogeneous soil and land-cover properties, how to consider entrainment from the free troposphere down to the surface layer, or how to parameterize these effects and their dependence on model resolution.

Since turbulent mixing in the PBL is active over a range of scales that is typically much smaller than the resolution of gray-zone models, various approaches are used to parameterize this mixing from the surface to the free troposphere. Surface fluxes represent the lower boundary condition for these PBL schemes and interaction with them. Turbulence is parameterized using basically two approaches. The "local approach" allows for interaction of the turbulence between

AFFILIATIONS: Wulfmeyer, Behrendt, Lange, Metzendorf, Muppa, and Späth—Institute of Physics and Meteorology, University of Hohenheim, Stuttgart, Germany; Turner—Global Systems Division, NOAA/Earth System Research Laboratory, Boulder, Colorado; Baker and Meyers—Atmospheric Turbulence and Diffusion Division, NOAA/Air Resources Laboratory, Oak Ridge, Tennessee; Banta, Bonin, Brewer, and Choukulkar—Chemical Sciences Division, NOAA/Earth System Research Laboratory, Boulder, Colorado; Buban and Lee—Atmospheric Turbulence and Diffusion Division, NOAA/Air Resources Laboratory, Oak Ridge, Tennessee, and University of Oklahoma, and NOAA/National Severe Storms Laboratory, Cooperative Institute for Mesoscale Meteorological Studies, Norman, Oklahoma; Dumas—Atmospheric Turbulence and Diffusion Division, NOAA/Air Resources Laboratory, and Oak Ridge Associated Universities, Oak Ridge, Tennessee; Hardesty and Senff—Cooperative Institute for Research in Environmental Sciences, University of Colorado Boulder, Boulder, Colorado; Heus—Cleveland State University, Cleveland, Ohio; Ingwersen—Institute of Soil Science and Land Evaluation, University of Hohenheim, Stuttgart, Germany; Newsom—Pacific Northwest National Laboratory, Richland, Washington; Osman—University of Oklahoma, and NOAA/National Severe Storms Laboratory, Cooperative Institute for Mesoscale Meteorological Studies, Norman, Oklahoma; Raasch—Institute of Meteorology and Climatology, Leibniz University of Hannover, Hannover, Germany; Santanello—NASA Goddard Space Flight Center, Greenbelt, Maryland; Wagner—Space Science and Engineering Center, University of Wisconsin–Madison, Madison, Wisconsin; Weckwerth—Earth Observation Laboratory, National Center for Atmospheric Research, Boulder, Colorado
CORRESPONDING AUTHOR: Volker Wulfmeyer, volker.wulfmeyer@uni-hohenheim.de

The abstract for this article can be found in this issue, following the table of contents.
DOI:10.1175/BAMS-D-17-0009.1

In final form 16 January 2018

adjacent atmospheric levels only. In the "nonlocal approach," the interactions between a single level and multiple different levels are considered. The basis for both approaches is the estimation of the turbulent flux profiles by a function that is usually proportional to the vertical gradient of the transported variable. The coefficient of proportionality is the turbulent exchange coefficient, which is a function of the length scale, the velocity scale, and stability functions. Formulations of these functions depend on the approach and closure technique deployed (e.g., Mellor and Yamada 1982; Cuijpers and Holtslag 1998; Weng and Taylor 2003; Grisogono 2010). A relatively new method that integrates both the local and nonlocal approaches has been proposed by Siebesma and Teixera (2000). Here, an eddy-diffusivity model for the local mixing is combined with an advective mass-flux approach (Siebesma et al. 2007).

The performance of turbulence parameterizations was studied by various research teams (e.g., Banks et al. 2016; Tastula et al. 2016; Han et al. 2016; Sakradzija et al. 2016), but a general understanding has still not been achieved. Sensitivity studies indicate that the nonlocal approach is more suitable for the CBL and turbulence driven primarily by buoyancy (e.g., Pleim 2007). However, the vertical mixing is often too large resulting in an overestimation of the PBL depth (e.g., Coniglio et al. 2013; Cohen et al. 2015; Milovac et al. 2016). The major challenge of the local approach is the treatment of large eddies that redistribute significant amounts of energy over the entire PBL. Underestimation of this mixing process in local schemes can result in PBLs that are too shallow, too moist, and too cold, especially in the case of dry convection (e.g., Holtslag and Boville 1993; Cuijpers and Holtslag 1998; Teixeira and Cheinet 2004). Therefore, the local approach seems to be more suitable for shear turbulence in a weakly stable PBL (e.g., Mellor and Yamada 1982).

Milovac et al. (2016) showed a strong dependence of PBL structure and fluxes on the surface flux parameterization. Different PBL turbulence parameterizations and changes in the land surface model led to similar differences in water vapor mixing ratio of ~1–2 g kg^{-1} in the mixed layer. This variability is a matter of concern since it can clearly make the difference whether convection initiation occurs in the model or not (Crook 1996; Ducrocq et al. 2002). Therefore, in order to disentangle the role of surface and PBL fluxes and L–A feedback, a new, comprehensive observing strategy is necessary that provides a joint dataset of the soil–vegetation–atmosphere system.

These data must include the measurement of the mean vertical profiles of wind, temperature, and moisture; their gradients; and their turbulence fluctuations from the surface to the free troposphere. A dataset containing these observations would enable direct comparisons of simulated and measured flux profiles and their dependence on scaling variables; it would also facilitate the development of new similarity relationships for flux parameterizations (Wulfmeyer et al. 2016).

In the last decade, significant advances in ground-based remote sensing of the PBL have been realized, primarily using lidar systems [see Wulfmeyer et al. (2015a) for an overview]. These observations enable a novel class of field experiments that capitalize on the synergy of these remote sensing methods to measure the quantities needed to evaluate and improve land surface and turbulence parameterization schemes. In this work, we present the development and application of this sensor synergy in the LAFE. To the best of our knowledge, LAFE is the first field campaign dedicated to a comprehensive observation of L–A interaction and feedback. The scientific goals are introduced, and we discuss how these can be reached with the LAFE dataset. This is just a first step; ultimately, this type of field experiments needs to be conducted in different climate regimes in order to get a global insight in L–A feedback for the benefit of weather forecast, climate, and Earth system models.

PREVIOUS LAND–ATMOSPHERE FEEDBACK STUDIES. *Model studies*. The strong coupling of L–A processes and variables as well as the resulting challenges of corresponding measurements are depicted in the sidebar on "Land–atmosphere feedback" using the surface latent heat flux as an example. The latent heat flux depends not only on soil temperature and moisture, vegetation properties, and temperature and moisture profiles in the atmospheric surface layer, but also on the divergence of the latent heat flux profile in the PBL. This complex web of interactions poses great challenges in the understanding, modeling, and measurement of L–A feedback. From the "Land–atmosphere feedback" sidebar, it is evident that L–A feedback is the result of the two-way interaction of soil–vegetation–atmospheric variables, which can be used to distinguish between the terms "interaction" and "feedback." The sidebar also demonstrates that a full observational characterization of L–A feedback requires the measurement of mean profiles of soil, land cover, and atmospheric variables; their vertical gradients; and the surface and entrainment fluxes.

Various research strategies have been proposed to characterize L–A interactions. Many of these

have been developed by the GEWEX LoCo initiative (Santanello et al. 2018). For example, Ek and Holtslag (2004) used a coupled 1D land surface–PBL model to investigate the role of soil moisture on cloud development in terms of a relative humidity tendency equation at the top of the PBL. This study demonstrated that understanding the L–A feedback requires measurements of entrainment fluxes. Findell and Eltahir (2003a) developed a framework based on a 1D coupled model to classify L–A coupling into regimes by using measures of convective triggering potential and humidity. To address model deficiencies, Santanello et al. (2009, 2011, 2013) developed and studied L–A coupling strength over the southern Great Plains in the United States, which highlighted the importance of entrainment quantification. Koster et al. (2006) and Seneviratne et al. (2006) used GLACE data from 12 forecast and regional climate models to define dry, transitional, and wet climate/soil moisture regimes based on the impact of soil moisture on the evapotranspiration variability. Using the same data, Guo et al. (2006) showed that most of the differences between the models and within a given model are associated with the surface water evaporation rate, which varies strongly and consistently with soil moisture trends and affects the L–A coupling strength. Dirmeyer et al. (2012) approached these feedbacks in terms of terrestrial versus atmospheric legs of LA coupling. Hohenegger et al. (2009) and Knist et al. (2016) showed that L–A coupling is sensitive not only to the model physics but also to the model grid increment.

LAND–ATMOSPHERE FEEDBACK ILLUSTRATED USING THE WATER-VAPOR FLUX PROFILE

The interaction of the land surface and the atmosphere is demonstrated here using typical states of the L–A system in an afternoon where a convective, entrainment-drying planetary boundary layer interacts with a negative slope of the virtual potential temperature θ_v in the surface layer. The drying is due to a water-vapor flux profile $\langle w'q'\rangle$(z), which has a positive slope (i.e., increases with height).

For the atmosphere (Fig. SB1), the evolution of the specific humidity q is described by the following prognostic equation:

$$\frac{\partial q}{\partial t} + \mathbf{V}\nabla q \cong -\frac{\partial}{\partial z}\langle w'q'\rangle.$$

For the land–atmosphere interface (Fig. SB2), we have

$$\langle w'q'\rangle_{\text{surface}} \cong -K\frac{\partial q}{\partial z} \cong C_{\text{wv}} r^{-1}\left[q^*_{\text{sat}}\left(T_{s,v}\right) - q\right].$$

The evolution of the fluxes at the L–A interface is described by the SEB and the relation of the latent heat flux with soil, vegetation, and soil properties. This can be approximated by a flux–gradient relationship, where K is the turbulent exchange coefficient, Cwv is the bulk exchange coefficient, r is the canopy and aerodynamic resistance, q^*_{sat} is the soil and canopy saturation specifc humidity evolution, and $T_{s,v}$ is the temperature of the bare soil ($_s$) or vegetation ($_v$).

For the soil layer (Fig. SB3), the temperature and moisture potential profiles are given by the heat conductivity equation and Darcy's law (not shown). The resulting profiles are coupled with the equation above for the surface latent heat flux.

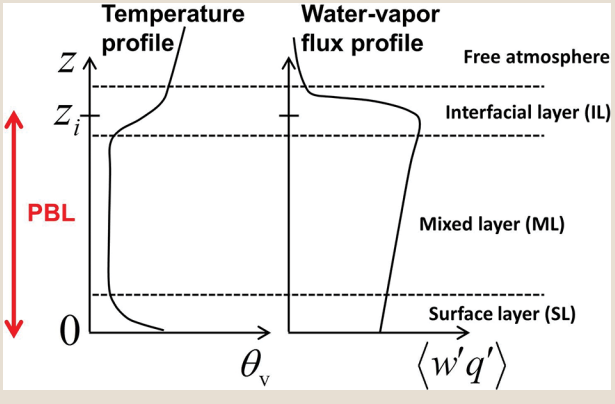

Fig. SB1. Structure of the CBL.

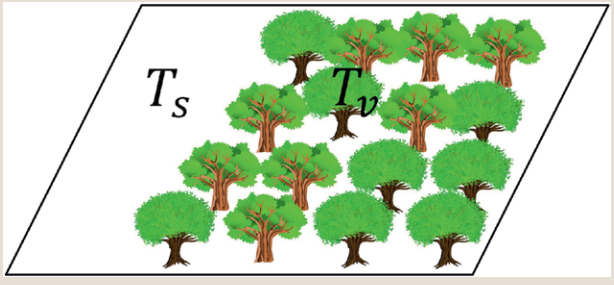

Fig. SB2. Bare soil and canopy interface.

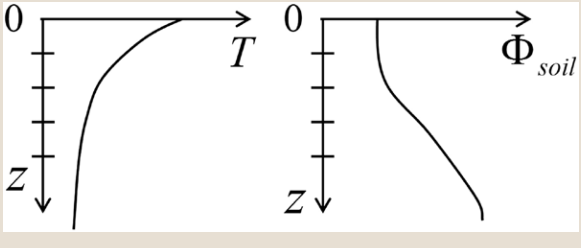

Fig. SB3. Soil temperature and moisture profiles.

Observational studies and field campaigns. Models are only as good as the data that were used for their development and verification. Currently, our understanding of L–A feedback processes is strongly impeded by the lack of suitable observations. Therefore, it is important to develop a comprehensive observation strategy for L–A feedback studies, which must involve the simultaneous measurements of the variables of all components and the transport processes between them.

Observational data have already been used to study the fidelity of L–A feedback within numerical models. As for the modeling studies, many of these statistically based approaches are summarized by Santanello et al. (2018) and the LoCo-based research efforts. Findell and Eltahir (2003b) investigated feedback between soil moisture and moist convection over the continental United States using radiosonde measurements. Ferguson and Wood (2011) used a 7-yr satellite remote sensing data record and available radiosonde measurements to produce global maps of L–A coupling signals. Roundy et al. (2013) investigated L–A feedbacks on diurnal time scales using satellite remote sensing data. Guillod et al. (2015) analyzed spatial and temporal soil moisture effects on afternoon rainfall by combining available satellite data for precipitation, soil moisture, total evaporative stress, and radiation with data gaps filled with GPCP and ERA-Interim data. They found that positive feedbacks between soil moisture and precipitation dominate in time, but rain more often occurs over drier soils. These studies only investigated relatively small portions of the L–A feedback process chain, primarily owing to the inability of the observations used to fully characterize all of the needed components of the L–A system.

Refined and more detailed studies of PBL turbulence and L–A feedback during field campaigns are now possible because a more sophisticated synergy of instruments is available. Likely the first campaign dedicated to L–A feedback was FIFE, which was conducted in Kansas between 1987 and 1989. FIFE already considered the important role of vegetation and applied a sophisticated combination of remote sensing and in situ instruments on various platforms (Sellers et al. 1988). Further studies covered other key regions for L–A feedback such as HAPEX-Sahel (Goutorbe et al. 1994) and the extensive BOREAS conducted in central Canada mainly between 1993 and 1996 (Hall 1999). More remote sensors were applied, such as during IHOP_2002 along the central U.S. dryline in 2002 (Weckwerth et al. 2004), LITFASS around the DWD Lindenberg Observatory during 2003 (Beyrich et al. 2006), COPS performed over the low-mountain Black Forest area in Germany in 2007 (Wulfmeyer et al. 2011), the BLLAST experiment performed in southern France in 2011 (Lothon et al. 2014), HOPE performed in heterogeneous midlatitude terrain in Germany in 2013 (Macke et al. 2017), and the ScaleX campaign on scale-crossing land surface and boundary layer processes in a pre-Alpine observatory between 2015 and 2016 (Wolf et al. 2017); the study areas became even more complex, PBL transition periods were included, and were among the first to use scanning active remote sensing systems.

Furthermore, multiyear, high-resolution datasets are available and used to look at turbulent properties of the PBL (e.g., Turner et al. 2014b; Berg et al. 2017; Osman et al. 2018) from the ARM observations at the SGP (Sisterson et al. 2016) and TWP (Long et al. 2016) sites as well as various observatories such as Cabauw in the Netherlands and Lindenberg in Germany. However, during these campaigns and observations, limited knowledge about the 3D structure of the PBL and the interaction of surface and entrainment fluxes was acquired, calling for more sophisticated approaches and instruments.

Observational gaps and new observations. To fully characterize L–A interactions, observations are needed in the soil, in the vegetation canopy, and from the surface layer to the top of the PBL. Measurements of temperature and moisture in the soil, as a function of depth from the surface to many tens of centimeters deep, are required to characterize the evolution of the land conditions. These characteristics are a strong function of soil texture and hydraulic coefficients. These observations need to be accompanied by the specification of vegetation parameters such as plant type, leaf area index, and canopy height as the vegetation can often provide a more efficient pathway to transfer water from the soil to the atmosphere. Observations of the energy balance above the canopy level are necessary, which includes the measurement of the ground net radiative flux, latent heat flux, and sensible heat flux. These observations are traditionally made by SEB stations that include the upwelling and downwelling surface longwave and shortwave radiative fluxes.

Measurements of PBL dynamics and thermodynamics are particularly critical to fully understand and characterize the L–A feedback. In the past, PBL and entrainment fluxes have been mainly determined by aircraft in situ measurements (e.g., Lenschow et al. 1994), a relatively sparse and expensive method.

Moreover, with in situ sensors, it is challenging to measure profiles of mean and turbulent quantities throughout the PBL, which is essential for evaluating new flux–gradient relationships and turbulence parameterizations. The lack of high-resolution temperature and water vapor profiles, their gradients, and their turbulent fluctuations is currently a major weakness for monitoring the CBL diurnal cycle and feedback processes. This is also a severe limitation of current satellite-based retrievals of PBL properties (Wulfmeyer et al. 2015a).

Ground-based lidars have become an important and emerging tool for turbulence profiling, as the high temporal and vertical resolution of these observations allow both the mean and higher-order-moment profiles to be observed. DLID systems can profile mean winds very accurately (e.g., Klein et al. 2015; Päschke et al. 2015) and are able to provide profiles of higher-order turbulent moments of the vertical wind and dissipation (e.g., Wulfmeyer and Janjić 2005; Ansmann et al. 2010; Lenschow et al. 2012; Berg et al. 2017). Water vapor can be remotely sensed with both WVDIAL (e.g., Wagner et al. 2013) and WVRLID (Turner et al. 2002; Whiteman 2003a,b; Froidevaux et al. 2013); both of these techniques have been shown to resolve turbulent fluctuations (second to fourth moments) in the water vapor field in the CBL (Wulfmeyer 1999a; Wulfmeyer et al. 2010; Turner et al. 2014a,b; Muppa et al. 2016; Di Girolamo et al. 2017). Simultaneous observations with DLID or radio acoustic sounding systems in the same volume can provide profiles of latent heat flux as well as stability indices (Senff et al. 1994; Wulfmeyer 1999b; Giez et al. 1999; Kiemle et al. 2007; Linné et al. 2007; Behrendt et al. 2011; Corsmeier et al. 2011). The capability of the WVRLID and DLID combination collocated at the ARM SGP site is demonstrated in Fig. 1. The left panel shows latent heat flux profiles measured using the eddy covariance technique, and the right panel the corresponding variance profiles of moisture and vertical wind. Noise and sampling error bars are also shown.

Temperature profiles can be observed with rotational TRLID (Radlach et al. 2008; Newsom et al. 2013; Hammann et al. 2015). A particularly exciting advance is the recent ability to observe profiles of turbulent temperature fluctuations (Behrendt et al. 2015) and the measurement of sensible heat flux profiles by combined observations with DLID (Wulfmeyer et al. 2015b). To our knowledge, this was the first time profiles of sensible heat flux have been derived in the PBL with lidar systems.

While operational lidars, such as those at the ARM SGP site, are able to provide long-term measurements of turbulent profiles (Turner et al. 2014b; Berg et al. 2017), one of the weaknesses of these datasets is that the near-surface level (lowest 100 m) is not well sampled. Optical scanners can make lidar measurements in different directions and improve the sampling of the surface layer of the PBL (i.e., the lowest 100 m). Precise measurements of the mean wind using multiple scanning Doppler lidars has been demonstrated in the XPIA field study (Lundquist et al. 2017) and the ScaleX campaign (Wolf et al. 2017). Using multi-Doppler techniques, high-temporal- and high-spatial-resolution wind measurements very close to the surface are possible.

Surface-layer temperature and water vapor measurements are also possible using scanning lidar systems and have been analyzed in Froidevaux

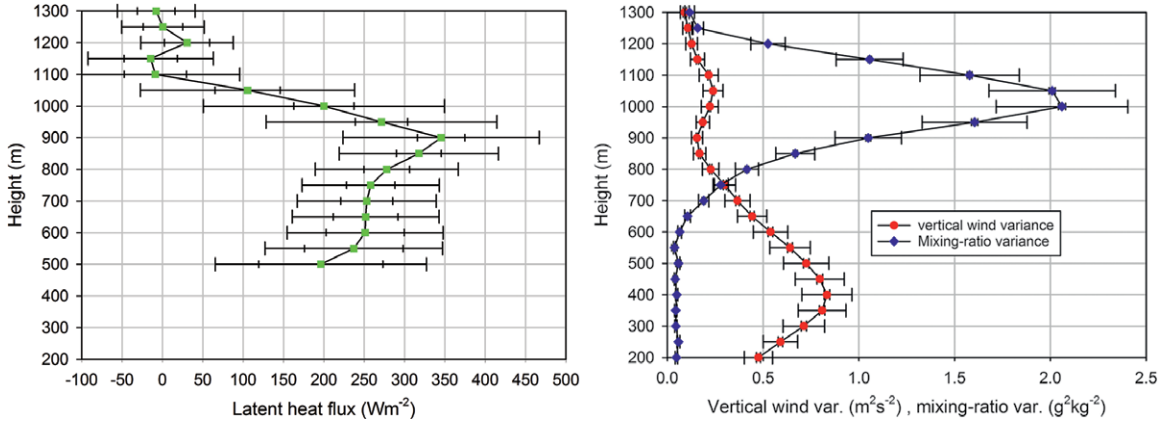

Fig. 1. (left) Latent heat flux profile measured at the ARM SGP site from 1856 to 2049 UTC 9 Nov 2012 with SRLID and a collocated DLID including noise (small caps) and sampling error bars (large caps). Lower-level flux measurements are possible but are still under investigation. (right) The corresponding vertical wind and mixing ratio variance profiles.

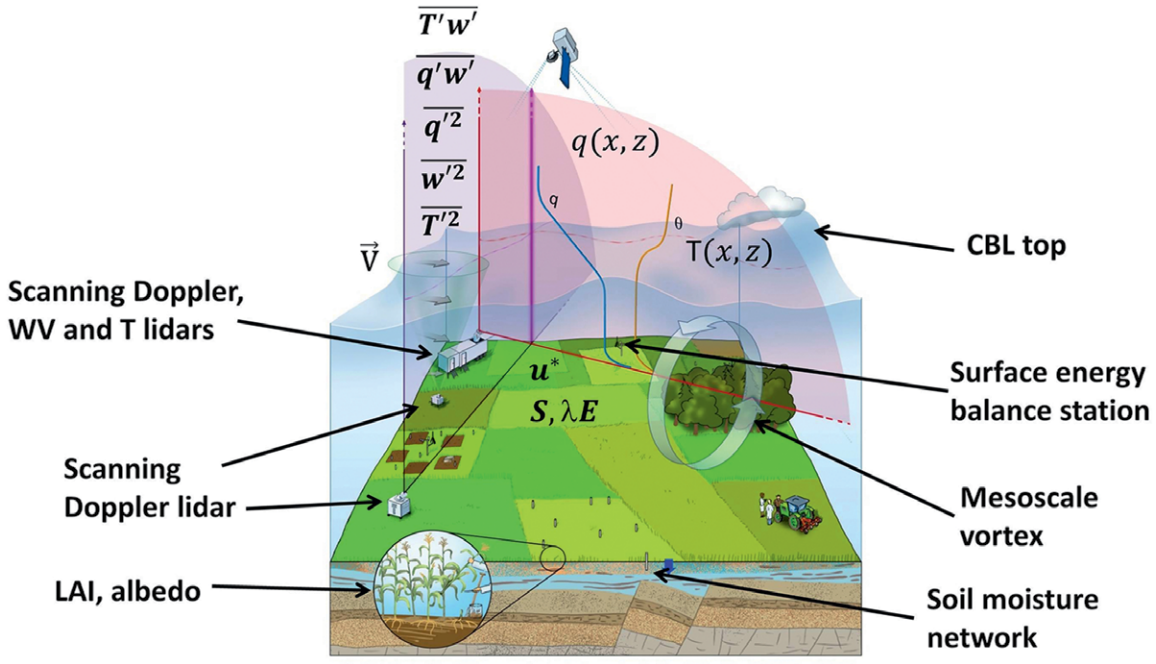

Fig. 2. The proposed concept for the combination of remote sensing systems enabling for the first time the simultaneous remote sensing of surface and entrainment fluxes. With the low-level scans, the friction velocity u^* and the surface sensible and latent heat flux S and λE will be determined in combination with the vertical profiles of specific humidity q and temperature T as well as their higher-order moments and fluxes. A conical scanning Doppler lidar allows for measuring the horizontal wind profile V.

et al. (2013), Hammann et al. (2015), and Späth et al. (2016). The latter team demonstrated that surface-layer profiles can be measured with vertical resolutions of a few meters as well as accuracies of 0.1 g kg^{-1} and 0.2 K up to a range of several kilometers. Furthermore, they showed the capability of the WVDIAL to measure 3D water vapor fields in the lower troposphere with high spatial and temporal resolutions. With these recent advances including the potential to measure entrainment fluxes of heat and moisture, it is timely to develop new concepts for producing original, synergetic datasets for studying L–A feedback.

THE LAND–ATMOSPHERE FEEDBACK EXPERIMENT (LAFE). *Concept and overarching goals.* The previous considerations led to a new concept for L–A feedback experiments, which is depicted in Fig. 2. This configuration addresses the required combination of measurements for advanced studies of L–A feedback including the observation of the heterogeneity of land surface fluxes and entrainment at the CBL top. The sensor synergy consists of networks of surface and vegetation in situ sensors together with a combination of scanning lidar systems. At the central site, a combination of DLID, TRLID/WVRLID or WVDIAL systems is operating in vertically pointing mode and a similar combination of these systems is operating in surface scanning modes. If not all of these systems are available, they can switch between these modes. During vertically pointing operation, the lidar systems measure profiles of turbulent quantities and fluxes including entrainment in the CBL. The scanning capability down to the land surface provides high-resolution profiles in the surface layer and 2D surface measurements of latent and sensible heat fluxes over different land-cover and soil types. Thus, the heterogeneity of land surface fluxes can be captured in more detail, which is hard to achieve with energy balance station networks. During the UHOH SABLE 2014 campaign, a first attempt to demonstrate a part of this innovative sensor synergy and operation modes was made. The results were presented in Wulfmeyer et al. (2015b) and Späth et al. (2016).

Based on these achievements, a new campaign with an enhanced sensor synergy, LAFE, was performed in August 2017 at the reconfigured ARM SGP site in Oklahoma (Sisterson et al. 2016). LAFE represents an international collaboration of several U.S. institutions as well as various

universities in the United States and Germany. Further details are found in the LAFE science plan (www.arm.gov/publications/programdocs/doe-sc-arm-16-038.pdf). The overarching goals and the research strategy are summarized in the "LAFE goal and objectives" sidebar.

LAFE observational design. LAFE took advantage of the newly reconfigured ARM SGP site. Figure 3 shows the layout of the new SGP domain and, in particular, the location of AERIs (Knuteson et al. 2004a,b) and DLID systems at four new profiling extended facilities (red diamonds) that are located 40–50 km away from the central facility. This configuration will allow us to study the moisture budget by adding the 2D and turbulent flux measurements at the central facility (thick black line to the NE).

Table 1 provides an overview of the LAFE instrumentation. The main remote sensing system synergy consists of three scanning lidar systems combining vertical pointing with low-level RHI scanning measurements of temperature, humidity, and wind according to Fig. 2, with two additional wind profiling lidar systems that are also performing RHI scans across the primary RHI path to create virtual towers. The setup of the LAFE instrumentation around the SGP site is presented in Fig. 4 and consists of three components.

First LAFE component. The first component consists of mainly vertically pointing lidar systems (see Fig. 4), namely, the water vapor and temperature SRLID (Goldsmith et al. 1998; Turner and Goldsmith 1999; Turner et al. 2002; Ferrare et al. 2006; Newsom et al. 2009; Wulfmeyer et al. 2010; Newsom et al. 2013; Turner et al. 2014a,b; Turner et al. 2016), SDLID (e.g., Hogan et al. 2009; Klein et al. 2015; Berg et al. 2017), UDLID (Pearson et al. 2009) (see Fig. 5), and NDIAL (Spuler et al. 2015; Weckwerth et al. 2016).

SRLID and the SDLID were continuously operated in vertically pointing mode for deriving vertical turbulence as well as sensible and latent heat flux measurements. The UDLID performed a modified, continuous six-direction pointing mode for studying TKE, momentum flux, and horizontal wind profiles (Bonin et al. 2017) that are essential for studying similarity relationships and parameterizations of turbulence.

NDIAL was located mainly upstream of the SGP site with a 915-MHz wind profiler in order to study the heterogeneity of the moisture field and moisture advection (see Fig. 3). This deployment strategy allows us to study inhomogeneities in the water vapor field due to advection at three different scales: at ~100 km by the network of four AERIs/DLIDs at the boundary facilities, along the 15-km distance between the NDIAL and the SRL, and along the 4-km RHI path observed by scanning lidar systems at the SGP site.

Second LAFE component. The second component employs a synergy of scanning lidar systems as well as surface and airborne in situ measurements (see Fig. 4). The high-resolution NOAA DLID, UDIAL (Wagner et al. 2013; Muppa et al. 2016; Späth et al. 2016), and URLID (Hammann et al. 2015; Behrendt et al. 2015) were operated (see Fig. 5). These lidars were placed in the northeastern corner of the ARM SGP central facility and scanned toward the northeast (purple and white planes in Figs. 2 and 4, respectively). Continuous RHI scans were performed for measuring the LOS velocity, the humidity, and the

LAFE GOAL AND OBJECTIVES

The overarching goal of LAFE is the study of L–A feedback in the SGP region containing different vegetation types and soil moisture conditions during summertime. Specifically, LAFE has four scientific objectives:

1) determine profiles of turbulent moments and fluxes and investigate new similarity relationships among gradients, variances, and fluxes.
2) map surface momentum, sensible heat, and latent heat fluxes using a synergy of scanning wind, humidity, and temperature lidar systems;
3) characterize L–A feedback and the moisture budget at the SGP site in dependence of different soil moisture regimes; and
4) verify LES and improve turbulence parameterizations in mesoscale models.

These objectives are addressed by the combination of the three LAFE sensor synergy components, which are presented in the "LAFE observational design" section and Table 1. The matrix of variables produced by LAFE is shown in Table 2. The research approaches to reach these four objectives and first results are demonstrated in the "Strategy to reach the objectives of LAFE" section.

LAFE is considered a starting point of a series of complementary field campaigns and configurations of observatories in different climate regions. LAFE will also contribute to national and international activities such as the HD(CP)^2 project in Germany, GLASS, the GEWEX LoCo initiative of the World Climate Research Programme (WCRP), and the L–A studies within DOE's ASR program.

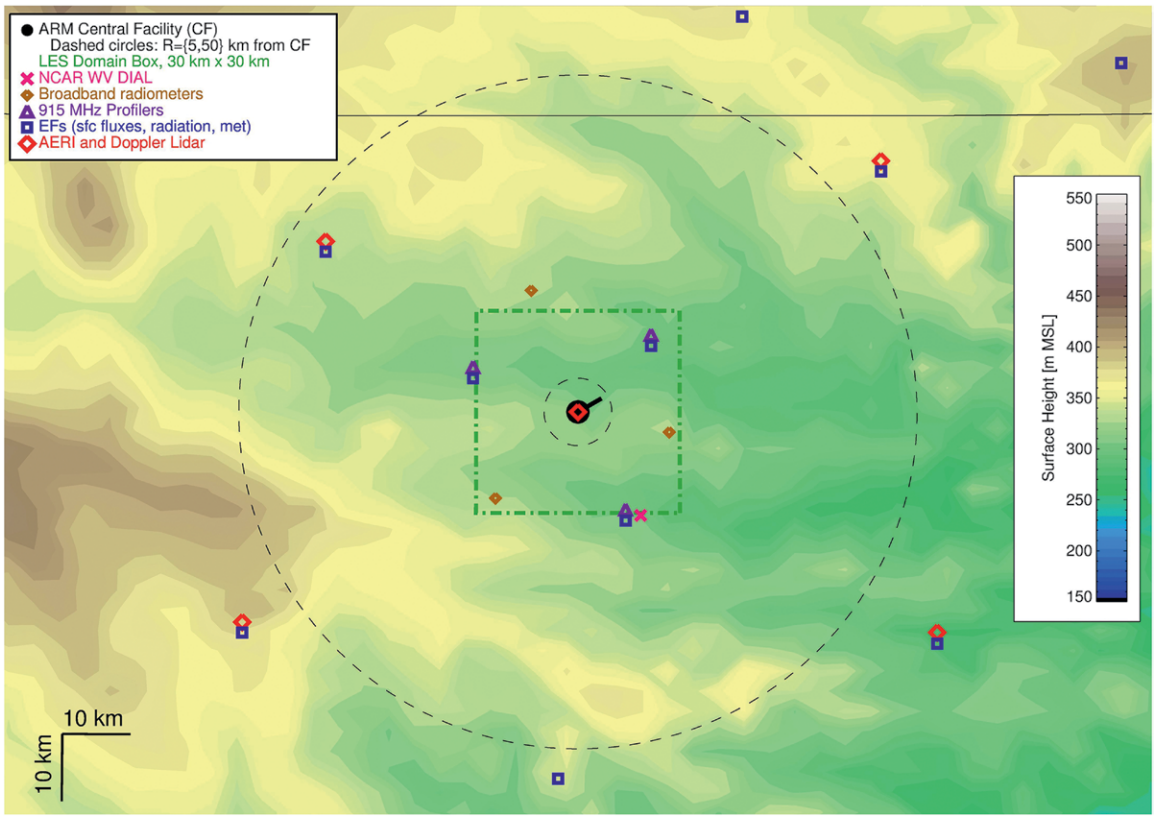

Fig. 3. The layout of the SGP site in Aug 2017 together with the surface elevation map of the region. The central LAFE instrumentation was deployed along the thick black line emanating from the central facility to the northeast (see Fig. 4). The four profiling extended facilities (red diamonds) that are approximately 50 km from the central facility, together with the NDIAL that was collocated with the 915-MHz wind profiler about 16 km south-southeast of the central facility, will provide critical information on water vapor and temperature advection. The multiple surface energy balance stations (blue squares) will be used to quantify radiation, momentum, latent heat, and sensible heat fluxes over different surface types.

temperature in a well-defined plane from the CBL top down to the canopy level. Furthermore, this component was complemented by three SEB towers from NOAA/ATDD (see Fig. 6) and one SEB station from UHOH (Wizemann et al. 2015). All four of these SEB towers included soil moisture and soil temperature measurements and were placed in a line at four locations with different field types under the RHI path. Each of the three ATDD towers included flux measurements at two heights (2 and 10 m AGL) to quantify flux divergence in addition to the standard meteorological measurements.

NOAA/ATDD also operated two sUAS, including the octocopter shown in Fig. 6 to obtain additional information on the spatial and vertical variability of temperature and humidity. A DJI S-1000 and a microdrone MD4–1000 sUAS were flown in two modes. Mode 1 was a vertical profiling mode to capture the rapid evolution of temperature and humidity from near the surface to its maximum allowed flight altitude of ~365 m AGL. The sUAS flew close to tower 2 when in this mode. Mode 2 involved flight at constant altitude between points adjacent to towers 2 and 3. These flights mapped the horizontal variability of air temperature and humidity as well as land surface temperature using an infrared camera and are being used to derive surface sensible heat fluxes following a recently developed technique by Lee et al. (2017) as well as the approach introduced in Morrison et al. (2017). These sUASs help to identify any coherent spatial structures that may not be easily identifiable from the measurements made at the four towers. The horizontal legs were made at a small number of flight levels (e.g., 100 and 300 m AGL).

Third LAFE component. The third component consists of two facilities deployed at different

Table 1. Overview of key instruments that participated in LAFE. All lidars also measured atmospheric backscatter and extinction profiles as well as cloud properties at their corresponding wavelengths.

Instrument	Institution	Methodology	Measured variables
PBL humidity			
UDIAL	IPM UHOH	3D scanning water vapor differential absorption lidar	3D fields of absolute humidity
NDIAL	NCAR	Vertically pointing water vapor differential absorption lidar	Vertical profiles of absolute humidity
3D scanning WVRLID (URLID)	IPM UHOH	3D scanning water vapor Raman lidar	3D fields of water vapor mixing ratio
SRLID	ARM	Vertically pointing water vapor Raman lidar	Vertical profiles of water vapor mixing ratio
AERI	ARM network and at SGP site, NOAA/NSSL in CLAMPS, SSEC in SPARC	Vertically pointing FTIR spectrometer	Vertical profiles of water vapor mixing ratio
sUAS DJI S-1000 and microdrone MD4–1000	NOAA/ARL ATDD	In situ	Air temperature, surface temperature (DJI S-1000 only), and relative humidity along flight path
PBL temperature			
3D scanning TRLID (URLID)	IPM UHOH	3D scanning temperature rotational Raman lidar	3D fields of temperature
SRLID	ARM	Vertically pointing temperature rotational Raman lidar	Vertical profiles of temperature
AERI	ARM network and at SGP site, NOAA NSSL in CLAMPS, SSEC in SPARC	Vertically pointing FTIR spectrometer	Vertical profiles of temperature
sUAS DJI S-1000 and microdrone MD4–1000	NOAA/ARL ATDD	In situ	Temperature along flight path
PBL wind			
NOAA DLID	NOAA/ESRL CSD	Leosphere Windcube 200S, 3D scanning coherent Doppler lidar	3D fields of LOS velocity
SPARC DLID	SSEC	HALO Photonics Streamline XR, 3D scanning coherent Doppler lidar	As above
CLAMPS DLID	NOAA/NSSL	As above	As above
SDLID	ARM	As above	As above, but operated mainly in vertically pointing mode
UDLID	IPM, UHOH	As above	As above, but operated in six-point scanning pointing mode, TKE, momentum flux, horizontal wind profile
Surface variables			
Flux tower	NOAA/ARL ATDD	In situ measurements at 2 and 10 m AGL	Standard meteorology, surface fluxes, soil temperature and moisture, radiation
Flux tower	IBS, UHOH	In situ measurements at 2 and 10 m AGL	Standard meteorology, surface fluxes, soil temperature and moisture, radiation
CLAMPS and SPARC	NOAA/NSSL, SSEC	In situ	Standard meteorology
sUAS DJI S-1000	NOAA/ARL ATDD	Passive remote sensing	Surface skin temperature, surface sensible heat flux
Piper Navajo	NOAA/ARL ATDD, UTSI	Downward-looking midinfrared camera	Surface skin temperature, vegetation indices in the VIS and NIR

distances near the RHI scan path, namely, SPARC (see Fig. 5) and the NOAA/NSSL CLAMPS (see Fig. 5). Both the SPARC and CLAMPS facilities contain a vertically pointing AERI and a scanning DLID. Both DLIDs were operated in a three-direction cross-track scanning pattern (such as in the upper-left corner of Fig. 2; see also Fig. 4). The primary objective for these two facilities is to perform dual-Doppler virtual towers with the NOAA DLID up to ~100 m above the SEB towers. SPARC sampled above towers 1, 2, and 3, whereas CLAMPS sampled above towers 2, 3, and 4. These DLID RHI scans realized crossing points of two DLID scans in different directions down to the surface in order to determine the wind profile over different land cover along the major LOS of the RHI scanning lidar systems. This is necessary for closing the MOST relationships. The XPIA field experiment demonstrated that these dual Doppler lidar scans do not need to be perfectly coordinated in time with the NOAA DLID if mean wind profiles are desired (Choukulkar et al. 2017), which greatly simplified operations. In addition, the SPARC includes an HSRL, which is also able to measure turbulent motions in the aerosol backscatter field (McNicholas and Turner 2014).

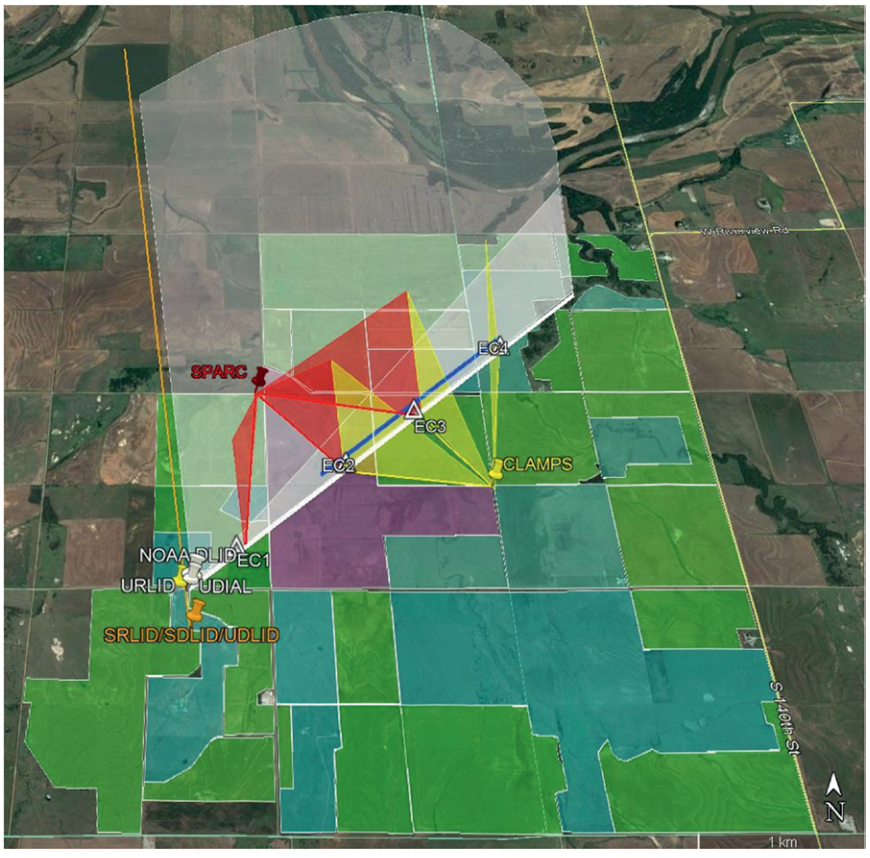

Fig. 4. The deployment and scanning strategy for LAFE at the ARM SGP central facility. The three scanning lidar systems (UDIAL, URLID, and NOAA DLID) were located 300 m north of the SRL and scanning in elevation above the main RHI (thick white line and planes). Four energy balance stations (including soil moisture and temperature) were installed at the tower locations 1–4 (EC1–4). Dual-Doppler lidar scans were also performed at these tower locations using a combination of the NOAA DLID and the DLIDs included with the SPARC (red planes) and CLAMPS (yellow planes). The sUAS flight track (blue) was parallel to the main RHI path. The field types are indicated by color: pasture (cyan), farm fields (which were mainly wheat stubble or soybeans; green), and conservation research program land (which has native grasses that are about 0.6 m tall; purple).

UTSI in cooperation with NOAA/ARL operated a Piper Navajo (see Fig. 6) manned fixed-wing aircraft to measure the surface temperature inhomogeneity over a large 10 km × 10 km area surrounding the ARM central facility. Its primary instrument is a downward-looking midinfrared camera. The Piper Navajo flew "lawnmower" patterns over this domain to fully characterize the surface conditions on 6 days during LAFE: 2 days at the beginning of the experiment, 2 days in the middle, and 2 days at the end. This allows the LAFE team to see how the overall soil and land-cover states evolved during the monthlong experiment and to determine the evolution of selected vegetation indices (e.g., the NDVI). On each selected day, the Piper Navajo flew three missions, in the early morning, around noon, and in the midafternoon. This sampling allows the LAFE team to characterize how the surface warms as the CBL grows as a result of insolation.

LAFE observation matrix. Table 2 presents a summary of the variables that were observed and will be derived by the LAFE sensor synergy. The key variables temperature T, water vapor mixing ratio m, absolute

Fig. 5. Key scanning lidar systems operated during LAFE. (top left) DLIDs operated in vertically staring or six-point scanning pointing modes collocated with the SRLID. (top right) Collocation of (left to right) the NOAA DLID, the URLID, and the UDIAL at the SGP central facility all pointing northeast. (bottom left) The SPARC and (bottom right) the CLAMPS systems deployed and operated close to the SGP central facility.

humidity ρ, and vertical wind w were measured with a temporal resolution of 1–10 s and a range resolution of 30–300 m. These lidar systems also observed aerosol particle backscatter and extinction coefficients, the aerosol optical thickness (β_{Par}, α_{Par}, τ_{Par}), and the instantaneous CBL depth z_i.

Furthermore, the horizontal wind profile V, the wind shear dV/dz, and the cloud optical thickness τ_C will be determined. From these results, the following variables will be derived: the *TKE* dissipation rate ε; profiles of the fluxes of water vapor (latent heat) and of its variance $\langle w'm' \rangle$, $\langle w'\rho' \rangle$, $\langle w'm'^2 \rangle$, and $\langle w'\rho'^2 \rangle$; the molecular destruction rates of humidity variances ε_m and ε_ρ; profiles of the temperature flux (sensible heat) and the flux of temperature variance $\langle w'T' \rangle$ and $\langle w'T'^2 \rangle$; and the molecular destruction rate of temperature variance ε_T. The errors will be specified with respect to noise and sampling errors according to Lenschow et al. (2000), Wulfmeyer et al. (2010), Turner et al. (2014b), and Wulfmeyer et al. (2016). The friction velocity u*; the surface latent and sensible heat fluxes λE and S will be derived with MOST (as long as it can be applied) and compared with the surface fluxes measured with the SEB stations. Then the convective velocity, humidity, and temperature scales w^*, q^*, and T^* can be deduced.

STRATEGY TO REACH THE OBJECTIVES OF LAFE AND FUTURE ADVANCED L–A FEEDBACK STUDIES.

Objective 1: Turbulence similarity relationships. For addressing objective 1, we are taking advantage of LAFE research component 1, the synergy between the SRLID, the SDLID, and the UDLID. Using water vapor and vertical velocity time series at different heights, their fluctuations can be measured with temporal resolutions of 1–10 s, typically. By means of the technique presented in Lenschow et al. (2000), these fluctuations are used to derive higher-order moments of mixing ratio and vertical velocity as well as their covariance, and thus the latent heat flux. Wulfmeyer et al. (2010) demonstrated that mixing ratio moments can be derived up to the third order from the SRLID with a temporal resolution of 30–60 min. Figure 1 confirms the potential of the SRLID–SDLID combination to measure latent heat flux and variance profiles with reasonable noise errors. During LAFE, considerably

more data were collected allowing for a deeper insight in the general capability of the SRLID–SDLID combination to measure latent heat flux profiles with sufficiently low noise and sampling errors. The SRLID temperature data will also be evaluated to see if accurate temperature variance and skewness as well as sensible heat flux profiling is possible (Newsom et al. 2013; Behrendt et al. 2015). Turner et al. (2014b) showed that the high stability and the nearly continuous operation of the SRLID allowed for first studies of the statistics of turbulent properties and how these depend on a variety of meteorological conditions. Thus, daily cycles of turbulent properties can be measured.

During several SOPs, comparisons of SRLID and UDIAL measurements were made. Figure 7 presents a simultaneous measurement of water vapor, temperature, and vertical wind time–height cross sections with resolutions of 10 s and 50–67.5 m, respectively. Clouds are marked by the black areas. Clearly the morning evolution of the CBL is resolved, and turbulent eddies below and around clouds are detected with high temporal and vertical correlation between all variables. These results demonstrate the high resolution and accuracy of active remote sensing for latent and sensible heat flux profiling.

A key scientific contribution of these data is the study of similarity relationships between gradients, variances, and fluxes. If these relations are verified and calibrated, they could represent the foundation of new turbulence parameterizations. Wulfmeyer et al. (2016) proposed how entrainment fluxes should depend on scaling variables in the interfacial layer such as the gradient Richardson number, which require the simultaneous measurement of wind shear and temperature gradients. For the first time, the LAFE dataset will provide the full information contents to verify these relationships. Similar relations can also be derived for variances and higher-order moments providing further ingredients for new turbulence parameterizations and studies of L–A feedback.

Objective 2: Remote sensing of surface fluxes. Objective 2 is addressed by combining the LAFE research components 2 and 3. The cross-RHI scans of the NOAA DLID and the SPARC and CLAMPS DLIDs will permit the measurement of wind profiles down to the surface at their crossing points (see Figs. 2 and 4). Simultaneously, the RHI scans of the UDIAL and the URLID will deliver temperature and moisture

Fig. 6. In situ and airborne instruments operated during LAFE. (top left) NOAA ATDD and (top right) UHOH SEB towers over soybeans and natural vegetation mix. (bottom left) The Piper Navajo at Ponca City airport. (bottom right) NOAA ATDD sUAS operating close to the SGP central facility.

profiles at these points as well. Consequently, along the LOS of the major RHI, the surface profiles and their gradient functions of wind, temperature, and moisture will be determined over the surface with different land-cover and soil characteristics. During LAFE, we will make the first attempt to use these

Table 2. Variables measured by the synergy of instruments during LAFE which includes SRLID, SDLID, NDIAL, URLID, UDIAL, NOAA DLID, and HSRL. The UDIAL, URLID and NOAA DLID systems performed coordinated RHI scans. The abbreviations are introduced in the text and in the list of acronyms.

Instrument	Temperature†	Humidity†	Wind	Fluxes, dissipation	Aerosols†	Clouds
SRLID	$T(z)$, dT/dz	$m(z)$, dm/dz, $m'(z)$, $\langle m'^2\rangle$, $\langle m'^3\rangle$			$\beta_{Par}(z)$, $\alpha_{Par}(z)$	Base, partly τ_C
UDIAL, vertical		$\rho(z)$, $d\rho/dz$, $\rho'(z)$, $\langle \rho'^2\rangle$, $\langle \rho'^3\rangle$, $\langle \rho'^4\rangle$			$\beta_{Par}(z)$	Base, partly τ_C
UDIAL, RHI		2D ρ, $d\rho/dz$ above canopy			2D $\beta_{Par}(z)$ field	2D cloud field
NDIAL		$\rho(z)$, $d\rho/dz$			$\beta_{Par}(z)$	Base
URLID, vertical	$T(z)$, dT/dz, $T'(z)$, $\langle T'^2\rangle$, $\langle T'^3\rangle$	$m(z)$, dm/dz, $m'(z)$, $\langle m'^2\rangle$			$\beta_{Par}(z)$, $\alpha_{Par}(z)$	Base, partly τ_C
URLID, RHI	2D T, dT/dz above canopy	2D m, dm/dz above canopy			2D $\beta_{Par}(z)$, $\alpha_{Par}(z)$ field	2D cloud field
SDLID, vertical			$w(z)$, $w'(z)$, $\langle w'^2\rangle$, $\langle w'^3\rangle$, ε		$\beta_{Par}(z)$	Base, partly τ_C
UDLID, six-direction mode			$V(z)$, dV/dz	TKE, $\langle v'w'\rangle$, $\langle u'w'\rangle$		
NOAA DLID, RHI			2D LOS wind field		2D $\beta_{Par}(z)$ field	2D cloud field
SRLID-SDLID, vertical				$\langle w'm'\rangle$, $d\langle w'm'\rangle/dz$, $\langle w'm'^2\rangle$, $\varepsilon_m^{\ddagger}$, $\langle w'T'\rangle$, $d\langle w'T'\rangle/dz$, $\langle w'T'^2\rangle$, $\varepsilon_T^{\ddagger}$		
UDIAL-NOAA DLID, vertical				$\langle w'\rho'\rangle$, $d\langle w'\rho'\rangle/dz$, $\langle w'\rho'^2\rangle$, $\varepsilon_m^{\ddagger}$		
URLID-NOAA DLID, vertical				$\langle w'T'\rangle$, $d\langle w'T'\rangle/dz$, $\langle w'T'^2\rangle$, $\varepsilon_T^{\ddagger}$		
Two DLID RHIs			u, v, and u^* at crossing points			
UDIAL-URLID, RHI				λE, S, $L^{\S}$		
NOAA DLID-UDIAL-URLID, RHIs			w^*, q^*, $T^{*\S}$			
AERI	$T(z)$	$m(z)$				Liquid water path, effective radius
DJI S-1000 sUAS	$T(z)$, dT/dz, T'	$m(z)$, dm/dz		$\langle w'T'\rangle$		
Microdrone MD4–1000 sUAS	$T(z)$, dT/dz, T'	$m(z)$, dm/dz		$\langle w'T'\rangle$		
Piper Navajo	Surface skin temperature					

† Also used to measure the instantaneous CBL depth z_i using dT/dz, dm/dz, $d\rho/dz$, and $d\beta_{Par}/dz$.

‡ The measurement of molecular destruction rates of variances is possible by evaluation of the autocovariance functions.

§ In combination with u^* measurements and MOST.

gradients to measure surface fluxes entirely with remote sensing systems at the SGP site. We operated NOAA DLID, UDIAL, and URLID in RHI scanning mode for full daily cycles under various surface and mesoscale forcing conditions as well as different cloud coverage. We will use a temporal resolution of 30–60 min and a spatial resolution of 30–300 m for the derivation of these fluxes provided that MOST will be applicable. The availability of this array of remote sensing instrumentation will be a unique opportunity to advance the understanding of boundary layer processes and their dependence on surface fluxes. The measurements of surface fluxes will be verified with the four SEB stations and other SEB and eddy covariance stations at the SGP site further complemented with surface radiation as well as soil moisture and temperature measurements.

The capability of the UDIAL to study the structure of the 2D water vapor field in the surface layer and the PBL is presented in Fig. 8. The data were collected during IOP 11 on 23 August 2017, which also included an evening transition. To study both the PBL structure and the surface layer with high vertical resolution, alternating 0°–90° RHIs for 10 min and 0°–7° RHIs for 50 min were performed. The top panel of Fig. 8 shows the measurement of the 2D water vapor field in the PBL. Various turbulent eddies and mesoscale structures were resolved up to a range of 4 km. The bottom panel of Fig. 8 presents a low-level RHI from the surface to 7°. Nearly continuously microscale to mesoscale coherent structures and/or turbulent eddies were observed, which entrained water

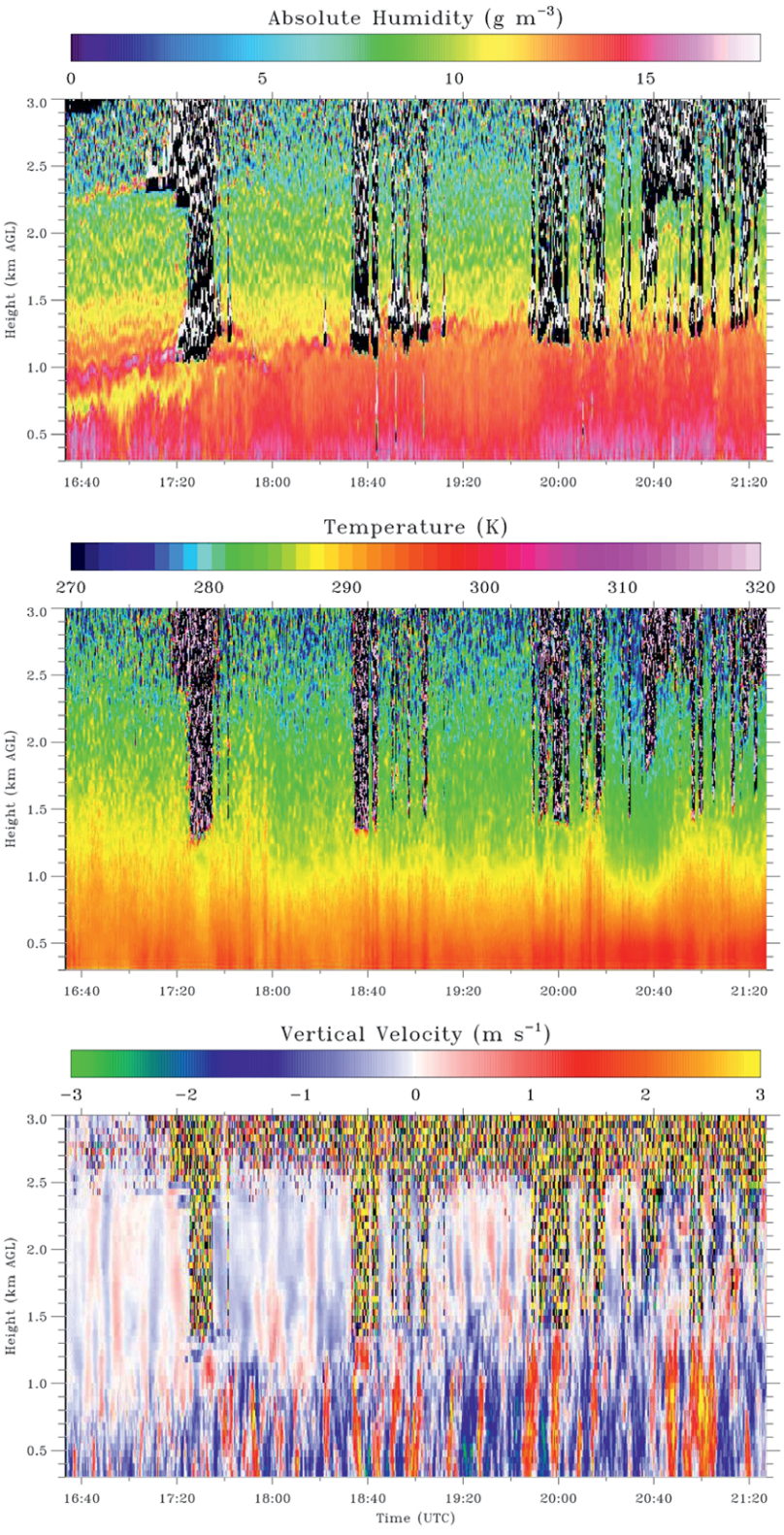

Fig. 7. Simultaneous measurements of water vapor, temperature, and vertical wind by UDIAL, URLID, and NOAA DLID during SOP2 on 26 Aug 2017. The temporal resolutions are 10 s. The vertical resolutions are 67.5 m for the UDIAL and URLID as well as 50 m for the DLID. Black areas are due to the presence of clouds, which can be partly penetrated by the URLID and the DLID.

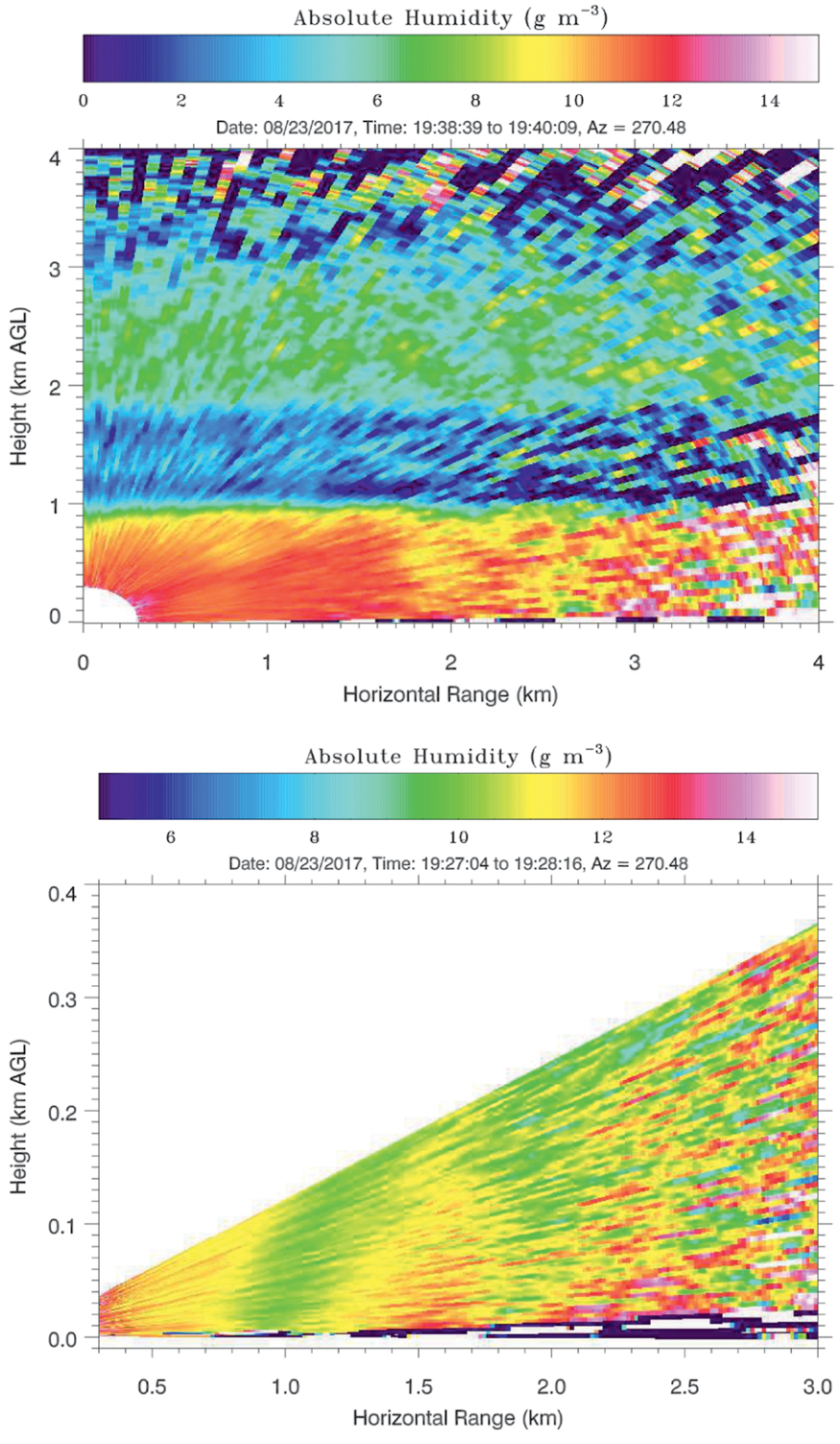

Fig. 8. Alternating RHI scans of the UDIAL for studying the 2D water vapor field performed during IOP11 on 23 Aug 2017. (top) The 0°–90° RHI with scan speed of 1° s^{-1} and a range resolution of 200 m showing several turbulent eddies from the surface up to the PBL top at approximately 900 m AGL. (bottom) The 0°–7° RHI with scan speed of 0.1° s^{-1} and also a range resolution of 200 m revealing several coherent structures in the surface water vapor field with an amplitude of ≈2 g m^{-3} ranging from turbulent to mesogamma scales.

vapor from the top of the PBL down to the surface.

The surface-layer profiles can be compared with gradient functions or their vertically integrated versions provided by MOST. There are two possibilities: either accurate fits to these functions will be realized, confirming MOST over different land-cover types, or deviations from MOST are detected, which would also be a very interesting scientific result motivating refinements of MOST in heterogeneous terrain.

Within LAFE, we hypothesize that the footprints of the soil and land cover at the crossing points are homogeneous enough so that MOST is valid. In this case, a fit to the gradient functions yields the surface friction velocity, the sensible and the latent heat fluxes, and the Monin–Obukhov length. As several crossing points are realized, insight on the spatial variability and the diurnal cycles of fluxes along the major RHI path is possible. However, the strong entrainment down to the surface and the presence of coherent mesoscale structures detected in Fig. 8 may question the applicability of MOST in heterogeneous terrain.

The LAFE strategy involved sampling the surface fluxes over different types of surfaces, and thus the in situ SEB stations were placed in fields with different plant covers (e.g., soybean plants and native grasses). The Bowen ratio (i.e., the ratio of the sensible

to the latent heat flux) can be markedly different over these different surface types. At the beginning of August 2017, the soil was relatively dry and thus the Bowen ratio was large; however, on 10–11 August, the SGP region received nearly 50 mm of precipitation, thus saturating the soil. Thus, by the end of the month, the Bowen ratio was significantly smaller than in the beginning of the month (Fig. 9). This variability in the surface fluxes provides a nice range of conditions for our analyses.

For 2 days during LAFE, the daily data-acquisition operations were expanded to include the evening transition period and to sample the nocturnal stable boundary layer and associated low-level jets (e.g., Banta 2008; Pichugina and Banta 2010). Figure 10 demonstrates the excellent information content of the six-point-scanning pointing mode of the UHOH DLID for providing the horizontal wind, TKE, and momentum flux profiles continuously during day and night. The evolution of the nocturnal jet can be studies as well as the morning transition and afternoon decay of TKE and momentum flux.

LAFE also captured a rare event: the solar eclipse of 2017. On 21 August, the sky was largely cloud-free when the moon moved across the face of the sun, resulting in about 89% obscuration during the peak of the eclipse. The large change in the downwelling shortwave flux modulated the other terms of the surface energy budget almost immediately, which then impacted the evolution of the PBL above (Turner

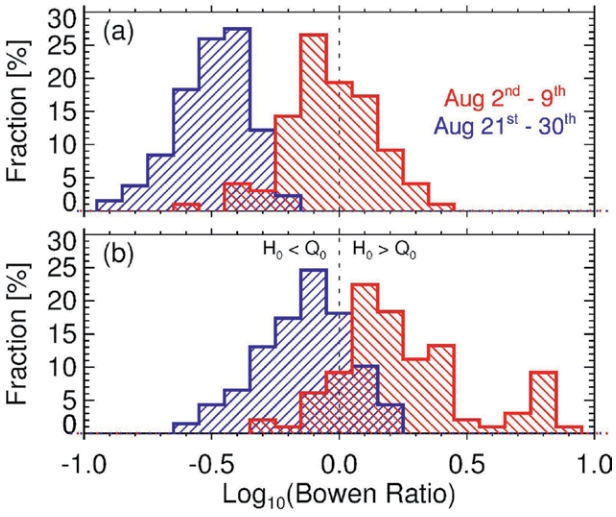

Fig. 9. The distribution of Bowen ratio measured over (a) a pasture and (b) a recently harvested wheat field during the early (red) and late (blue) parts of LAFE.

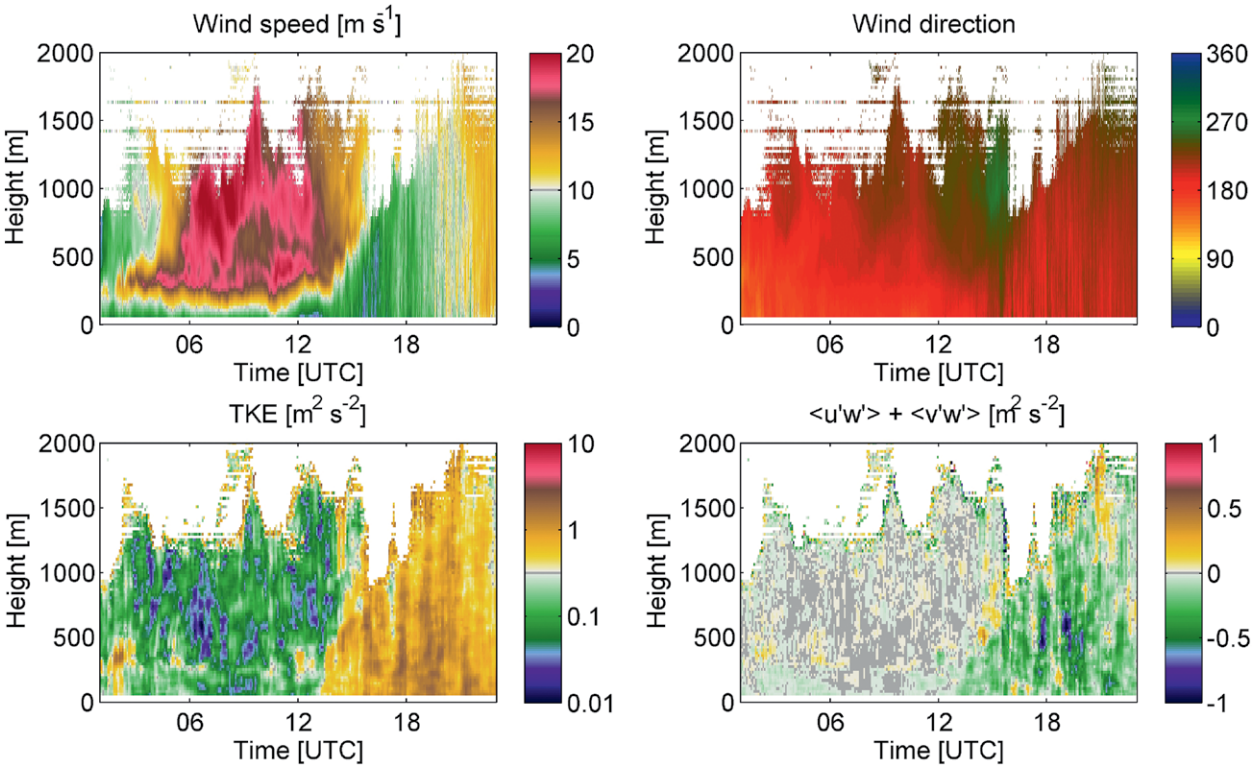

Fig. 10. Analysis of the six-point scanning pointing mode of the UHOH DLID demonstrating the large information contents of this technique. With this setup, horizontal wind, TKE, and momentum flux profiles can be simultaneously and continuously measured from the surface layer throughout the PBL including the interfacial layer. These measurements were performed during 16 Aug 2017.

Table 3. Model systems to be used for comparisons with LAFE data.

Model	Configuration	Horizontal grid increments	Turbulence parameterizations	Land surface and vegetation parameterization	Research center and reference
WRF-Noah-MP	LAM driven by ECMWF analysis with data assimilation	Mesoscale to turbulence permitting (100 m)	MYNN, YSU in the outer domains, none in the inner domain	MOST; Jarvis and Ball–Berry schemes	UHOH (Schwitalla et al. 2017)
WRF-Noah	Periodic LES with ensemble of large-scale forcings from data assimilation and analyses	100 m	None	prescribed surface fluxes from observations	ARM LASSO project (Gustafson et al. 2017a)[a]
HRRR	Hourly updated operational WRF-ARW-based model-driven 13-km RAP analyses	3 km	MYNN-EDMF	RUC LSM with MYNN surface	NOAA/ESRL GSD (Benjamin et al. 2016)
PALM	Periodic LAM driven by ECMWF analyses	1–50 m	—	TESSEL scheme from ECMWF; MOST or surface layer fully resolved	Institute of Meteorology and Climatology, University of Hannover (Maronga et al. 2015)
DALES	Periodic LAM driven by ARM variational analysis	5–100 m	1.5-order TKE	MOST	Cleveland State University (Heus et al. 2010)
COMMAS	Periodic or specified boundaries from analyses	10–500 m	TKE closure scheme	MOST	NOAA/ARL (Buban et al. 2012)
ICON-LES	Global with grid refinement	156 m	Three dimensional, diagnostic Smagorinsky scheme	MOST; plant-type parameterization	Meteorological Institute, University of Bonn (Heinze et al. 2017)

[a] See www.arm.gov/capabilities/modeling/lasso.

et al. 2018). This "rapid sunset/sunrise" event makes an excellent complement to the observations collected during the normal evening/morning transition times and should prove extremely useful in teasing out the details of L–A interactions and feedbacks.

Objective 3: Feedbacks and budgets. The combination of variables measured during LAFE, together with the temporal and vertical resolution of these observations, makes the estimation of the water vapor mean and variance budgets possible (see Table 2). Crucial parts of these budgets are the advection terms, which are very difficult to measure. Michael (1994) and Higgins et al. (2013) demonstrated the potential of scanning lidar systems for improving the estimation of advection. The LAFE design will enable us to estimate this component with improved accuracy. The 3D moisture gradient on different spatial scales will be determined using the AERI at the ARM central facility as well as the AERI and DLIDs that are part of the new SGP boundary facility network (Figs. 3 and 4). The RHI scans of the UDIAL in combination with the NOAA DLID will measure the horizontal water vapor gradient along the LOS of RHI on scales up to 4 km, whereas the NDIAL and the 915-MHz profiler will observe scales between the two above. Furthermore, the horizontal wind measurements of the UDLID, the combination of the other DLIDs used during LAFE, and adding other wind profile measurements at the SGP site will be used to get the best estimate of the horizontal wind profile.

Observations of advection, the PBL budget, and entrainment processes are key to understanding the full nature of L–A coupling and assessing model physics (e.g., LSM and PBL schemes) in interactive mode. Research as part of the LoCo project has demonstrated this, where the mixing diagram approaches of Betts (1992) and Santanello et al. (2009) are used to simultaneously quantify the behavior of surface fluxes (latent, sensible), PBL fluxes (entrainment, advection), and states (2-m temperature, humidity). However, these diagnostics have been limited in terms of model evaluation or development due to lack of

PBL height, advection, and entrainment observations. The measurements proposed herein would thus have immediate impact on LoCo research by providing detailed insight as to where the development needs to be targeted.

Objective 4: Verification of LES and mesoscale models. Objective 4 will evaluate turbulence parameterizations and perform model verification. An example for the parameterizations of entrainment fluxes and variances is presented in Wulfmeyer et al. (2016). Validation and refinement of flux–gradient relationships will eventually lead to advanced parameterizations of CBL turbulent fluxes and land surface fluxes in mesoscale models. Various model runs and outputs will be compared with the LAFE measurements based on Table 2 and investigated with respect to their accuracy.

An overview of these models is presented in Table 3. We will take advantage of the ARM LASSO project (Gustafson et al. 2017b), which will become operational soon; LAFE is very timely for these kinds of comparisons and model verification efforts. Further model runs and comparisons are planned for mesoscale models such as using the hourly updated HRRR model (Benjamin et al. 2016) run operationally at the National Centers for Environmental Prediction and WRF-Noah-MP and for various LES models such as PALM (Maronga et al. 2015), DALES (Heus et al. 2010), and COMMAS. Within the WRF-Noah-MP configuration of UHOH, ensemble runs with different turbulence parameterizations will be performed over the SGP site. High-resolution PALM ensemble simulations (10 m or less) with varying initial perturbances will also help to better separate the signature caused by the land surface heterogeneities from the general turbulence. It is envisioned that the global ICON model of the DWD with turbulence-permitting grid refinement will also be run over the SGP domain.

Essential for the success of model verification is the extraction of all parameters and variables from mesoscale model runs necessary for dedicated comparisons with respect to surface fluxes and turbulence parameterizations. As these variables are typically not routinely provided, the model outputs will have to be extended. If these results become accessible, a huge ensemble of equations related to other local and nonlocal turbulence parameterizations as well as for parameterizations based on mass-flux schemes can be studied and improved.

From the LES model simulations, higher-order turbulent moment profiles and flux profiles will be determined and compared against the lidar and in situ observations. The results will also allow us to give more precise estimates of the uncertainty of the turbulence measurements (Sühring and Raasch 2013). A very useful example of DLID measurements that will be used to evaluate the evolution of the PBL in LES (and other model) simulations is presented in Fig. 10 (Sathe et al. 2015). These LES profiles are not parameterized save for a subfilter-scale contribution that should be small in the bulk of the boundary layer. While LES simulations have traditionally been used for idealized and theoretical studies, these simulations will be driven by reanalysis and observational data, following Neggers et al. (2012). The obvious advantage is that these simulations can be expected to be closer to the observations, at least in a statistical sense, helping to separate errors due to initial conditions and model physics. Relationships between surface fluxes, atmospheric turbulence, entrainment, and cloud formation found in the observations are likely to show up in these simulations as well, which would mean that the LES may serve as a virtual laboratory to test hypotheses. For instance, by breaking certain couplings in the L–A, one could deduce cause and effect for these feedbacks. LES could also assist in comparisons with validations of large-scale parameterizations. Indeed, the original premise behind the test bed setup (Neggers et al. 2012) was that parameterization schemes are usually designed against ideal and idealized datasets and may not hold as well against more realistic data. This is particularly true for parameterizations of the PBL and of PBL clouds.

There are many LES model components that share the same weaknesses found in mesoscale models. For instance, subgrid-scale turbulence is still parameterized, which causes uncertainties around stable interfaces such as the surface layer and the entrainment layer—especially for coarser LES resolutions (100 m and coarser). The surface layer would be of particular interest here. This is not only because interactive soil models are relatively new in LES, and can therefore likely be optimized for the smaller scales, but also because typical MOST-based surface-layer parameterizations may not be valid in very high-resolution simulations. Datasets like the LAFE measurements will therefore be invaluable to improve the surface and soil parameterizations of LES and larger-scale models.

SUMMARY AND OUTLOOK. In this work, we described key research activities for the improvement of the next generation of weather forecast, climate, and Earth system models. As the resolutions used in these model systems approach the gray

zone of turbulence, new and scalable combinations of the parameterization of surface fluxes and PBL turbulence in heterogeneous terrain need to be developed and tested. The deficiencies in current parameterizations have to be detected and suggestions for their improvement have to be made as these problems are leading to suboptimal representations of L–A feedback and, thus, to errors in the representation of the diurnal cycle of PBL dynamics and thermodynamics including the simulation of convection initiation. As these errors are significant, research on L–A feedback is a prerequisite for a better simulation of clouds and precipitation including extreme events and its climate statistics.

We have demonstrated that advanced insight in L–A interaction and feedback requires the application of new observations, as the whole L–A system needs to be investigated from the land surface throughout the PBL into the free troposphere including the effects of entrainment. We also showed that combined measurements of dynamical and thermodynamical fields are necessary.

This is now possible with the recent development of new instrumentation and a novel synergy of these instruments. This sensor synergy mainly consists of scanning active remote sensing systems, which are able to observe wind, temperature, and water vapor profiles with fine range and temporal resolutions so that gradients and turbulence can be measured simultaneously from the surface to the interfacial layer at the top of the PBL. These key instruments are water vapor DIAL, WVRLID, TRLID, and DLID. The synergy of these instruments also permits the observation of 2D fields of surface fluxes and vertical profiles of sensible and latent heat fluxes, which will be investigated in combination with soil and vegetation measurements. Thus, we demonstrated that we have now the tools not only to simulate but also to observe the gray zone of turbulence.

The application of this sensor synergy was realized and exploited during the LAFE conducted at the ARM SGP site during August 2017. We have described the setup and operational modes of these systems. To the best of our knowledge, LAFE is the first international field campaign dedicated to a direct and almost complete observation of L–A feedback without any model input.

Four objectives of LAFE have been defined and can be addressed with the LAFE dataset: 1) the determination of turbulence and latent heat flux profiles and the investigation of new similarity relationships for fluxes and variances, particularly with respect to entrainment; 2) the mapping of surface momentum, sensible heat, and latent heat fluxes; 3) the characterization of L–A feedback and the moisture budget in dependence of different soil moisture regimes; and 4) the verification of LES runs and the improvement of turbulence parameterizations in mesoscale models. Because of this general research approach, the instrument configuration presented here can serve as a bridge to advanced approaches to evaluate/improve satellite-based PBL monitoring and may be considered as a blueprint for a new generation of experiments conducted in different climate regions in order to achieve an improved representation of L–A feedback in models globally.

ACKNOWLEDGMENTS. This work is in memoriam of Prof. Dr. Zbigniew Sorbjan, who made significant contributions to the preparation of the research activities presented in this work. LAFE is funded by the DOE, NASA, and NOAA in the United States as well as the BMBF in Germany via the HD(CP)^2 project. Support concerning the preparation and performance of LAFE by the ARM program via Nicki Hickmon, Chris Martin, James Martin, Mike Ritsche, and John Schatz is highly appreciated. We acknowledge the support of LAFE by IPM UHOH staff, namely, Andrea Riede, Alexander Geißler, and Hans-Dieter Wizemann. We highly acknowledge the operation of the Piper Navajo aircraft by the UTSI team headed by Dr. Steve Brooks.

Furthermore, the field phase of LAFE was assisted by many students and scientists, particularly, Simon Kleine (UHOH); Justin Flaherty (Cleveland State University); Sarah Borg, Greg Blumberg, and Ryan Pajela (University of Oklahoma); and Coda Phillips and David Loveless (University of Wisconsin–Madison).

The data for this paper can be made available upon request from the authors. The LAFE data will be stored in the ARM data archive.

APPENDIX: LIST OF ACRONYMS.

1D, 2D, 3D	One-dimensional, two-dimensional, three-dimensional
AERI	Atmospheric Emitted Radiance Interferometer
AGL	Above ground level
ARL	Air Resources Laboratory
ARM	Atmospheric Radiation Measurement
ASR	Atmospheric System Research

ATDD	Atmospheric Turbulence and Diffusion Division
BLLAST	Boundary Layer Late Afternoon and Sunset Turbulence
BMBF	Federal Ministry of Education and Research of Germany
BOREAS	Boreal Ecosystem–Atmosphere Study
CBL	Convective planetary boundary layer
CIMMS	Cooperative Institute for Mesoscale Meteorological Studies
CIMSS	Cooperative Institute for Meteorological Satellite Studies
CIRES	Cooperative Institute for Research in Environmental Sciences
CLAMPS	Collaborative Lower Atmospheric Mobile Profiling System
COMMAS	Collaborative Model for Multiscale Atmospheric Simulation
COPS	Convective and Orographically Induced Precipitation Study
CSD	Chemical Sciences Division
DALES	Dutch Atmospheric LES
DIAL	Differential absorption lidar
DLID	Doppler lidar
DOE	Department of Energy
DWD	German Meteorological Service
EDMF	Eddy-diffusivity mass flux
ERA	ECMWF reanalyses
ERA-Interim	European Centre for Medium-Range Weather Forecasts (ECMWF) interim reanalysis
FIFE	First International Satellite Land Surface Climatology Project Field Experiment
GEWEX	Global Energy and Water Exchanges Project
GLACE	Global Land–Atmosphere Coupling Experiment
GLASS	Global Land–Atmosphere System Study
GPCP	Global Precipitation Climatology Project
GSFC	Goddard Space Flight Center
HAPEX	Hydrological Atmospheric Pilot Experiment
HD(CP)^2	High-Definition Clouds and Precipitation Project
HOPE	HD(CP)^2 Observational Prototype Experiment
HRRR	High-Resolution Rapid Refresh model
HSRL	High-spectral-resolution lidar
IBS	Institute of Soil Science and Land Evaluation at UHOH
ICON	Icosahedral nonhydrostatic (DWD model)
IHOP_2002	International H_2O Project
IL	Interfacial layer
IOP	Intensive observation period
IPM	Institute of Physics and Meteorology at UHOH
L–A	Land–atmosphere
LAFE	Land Atmosphere Feedback Experiment
LASSO	LES ARM Symbiotic Simulation and Observation
LES	Large-eddy simulation
Lidar	Light detection and ranging
LITFASS	Lindenberg Inhomogeneous Terrain–Fluxes between Atmosphere and Surface: A Long-Term Study
LoCo	Local coupling
LOS	Line of sight
LSM	Land surface model
MYNN	Mellor–Yamada–Nakanishi–Niino
MOST	Monin–Obhukov similarity theory
NASA	National Aeronautics and Space Administration
NCAR	National Center for Atmospheric Research
NDIAL	NCAR WVDIAL
NDVI	Normalized difference vegetation index

NOAA	National Oceanic and Atmospheric Administration
Noah-MP	Noah LSM with multiparameterization options
NSSL	National Severe Storms Laboratory
OU	University of Oklahoma
PALM	Parallelized LES Model
PBL	Planetary boundary layer
RAP	Rapid-Refresh model
RHI	Range–height indicator
RLID	Raman lidar
RRL	Rotational Raman lidar
RUC	Rapid update cycle
SABLE	Surface Atmospheric Boundary Layer Experiment
SDLID	SGP Doppler lidar
SEB	Surface energy balance
SGP	Southern Great Plains
SOP	Special observation period
SPARC	University of Wisconsin–Madison SSEC Portable Atmospheric Research Center
SRLID	SGP Raman lidar
SSEC	Space Science and Engineering Center
sUAS	Small unmanned aircraft system
TESSEL	Tiled ECMWF Scheme for Surface Exchanges over Land
TKE	Turbulent kinetic energy
TRLID	Temperature Raman lidar
TWP	Tropical western Pacific
UDIAL	UHOH WVDIAL
UDLID	UHOH Doppler lidar
UHOH	University of Hohenheim
URLID	UHOH temperature and water vapor Raman lidar
UTSI	University of Tennessee Space Institute
WCRP	World Climate Research Programme
WRF	Weather Research and Forecasting Model
WMO	World Meteorological Organization
WVDIAL	Water vapor differential absorption lidar
WVRLID	Water vapor Raman lidar
WWRP	World Weather Research Programme
YSU	Yonsei University

REFERENCES

Ansmann, A., J. Fruntke, and R. Engelmann, 2010: Updraft and downdraft characterization with Doppler lidar: Cloud-free versus cumuli-topped mixed layer. *Atmos. Chem. Phys.*, **10**, 7845–7858, https://doi.org/10.5194/acp-10-7845-2010.

Baklanov, A. A., and Coauthors, 2011: The nature, theory, and modeling of atmospheric planetary boundary layers. *Bull. Amer. Meteor. Soc.*, **92**, 123–128, https://doi.org/10.1175/2010BAMS2797.1.

Banks, R. F., J. Tiana-Alsina, J. M. Baldasano, F. Rocadenbosch, A. Papayannis, S. Solomos, and C. G. Tzanis, 2016: Sensitivity of boundary-layer variables to PBL schemes in the WRF model based on surface meteorological observations, lidar, and radiosondes during the HygrA-CD campaign. *Atmos. Res.*, **176–177**, 185–201, https://doi.org/10.1016/j.atmosres.2016.02.024.

Banta, R. M., 2008: Stable boundary layer regimes from the perspective of the low-level jet. *Acta Geophys.*, **56**, 58–87, https://doi.org/10.2478/s11600-007-0049-8.

Behrendt, A., and Coauthors, 2011: Observation of convection initiation processes with a suite of state-of-the-art research instruments during COPS IOP8b. *Quart. J. Roy. Meteor. Soc.*, **137**, 81–100, https://doi.org/10.1002/qj.758.

——, V. Wulfmeyer, E. Hammann, S. K. Muppa, and S. Pal, 2015: Profiles of second- to third-order moments of turbulent temperature fluctuations in the convective boundary layer: First measurements with

rotational Raman lidar. *Atmos. Chem. Phys.*, **15**, 5485–5500, https://doi.org/10.5194/acp-15-5485-2015.

Benjamin, S. G., and Coauthors, 2016: A North American hourly assimilation and model forecast cycle: The Rapid Refresh. *Mon. Wea. Rev.*, **144**, 1669–1694, https://doi.org/10.1175/MWR-D-15-0242.1.

Berg, L. K., R. K. Newsom, and D. D. Turner, 2017: Year-long vertical velocity statistics derived from Doppler lidar in the continental convective boundary layer. *J. Appl. Meteor. Climatol.*, **56**, 2441–2454, https://doi.org/10.1175/JAMC-D-16-0359.1.

Betts, A. K., 1992: FIFE atmospheric boundary-layer budget methods. *J. Geophys. Res.*, **97**, 18 523–18 531, https://doi.org/10.1029/91JD03172.

Beyrich, F., and Coauthors, 2006: Area-averaged surface fluxes over the Litfass region based on eddy-covariance measurements. *Bound.-Layer Meteor.*, **121**, 33–65, https://doi.org/10.1007/s10546-006-9052-x.

Bonin, T. A., and Coauthors, 2017: Evaluation of turbulence measurement techniques from a single Doppler lidar. *Atmos. Meas. Tech.*, **10**, 3021–3039, https://doi.org/10.5194/amt-10-3021-2017.

Boutle, I. A., J. E. J. Eyre, and A. P. Lock, 2014: Seamless stratocumulus simulation across the turbulent gray zone. *Mon. Wea. Rev.*, **142**, 1655–1668, https://doi.org/10.1175/MWR-D-13-00229.1.

Buban, M. S., C. L. Ziegler, E. R. Mansell, and Y. P. Richardson, 2012: Simulation of dryline misovortex dynamics and cumulus formation. *Mon. Wea. Rev.*, **140**, 3525–3551.

Choukulkar, A., and Coauthors, 2017: Evaluation of single and multiple Doppler lidar techniques to measure complex flow during the XPIA field campaign. *Atmos. Meas. Tech.*, **10**, 247–264, https://doi.org/10.5194/amt-10-247-2017.

Cohen, A. E., S. M. Cavallo, M. C. Coniglio, and H. E. Brooks, 2015: A review of planetary boundary layer parameterization schemes and their sensitivity in simulating southeastern U.S. cold season severe weather. *Wea. Forecasting*, **30**, 591–612, https://doi.org/10.1175/WAF-D-14-00105.1.

Coniglio, M. C., J. Correia, P. T. Marsh, and F. Kong, 2013: Verification of convection-allowing WRF model forecasts of the planetary boundary layer using sounding observations. *Wea. Forecasting*, **28**, 842–862, https://doi.org/10.1175/WAF-D-12-00103.1.

Corsmeier, U., and Coauthors, 2011: Driving processes for deep convection over complex terrain: A multi-scale analysis of observations from COPS-IOP 9c. *Quart. J. Roy. Meteor. Soc.*, **137**, 137–155, https://doi.org/10.1002/qj.754.

Crook, N. A., 1996: Sensitivity of moist convection forced by boundary layer processes to low-level thermodynamic fields. *Mon. Wea. Rev.*, **124**, 1767–1785, https://doi.org/10.1175/1520-0493(1996)124<1767:SOMCFB>2.0.CO;2.

Cuijpers, J. W. M., and A. A. M. Holtslag, 1998: Impact of skewness and nonlocal effects on scalar and buoyancy flux in convective boundary layers. *J. Atmos. Sci.*, **55**, 151–162, https://doi.org/10.1175/1520-0469(1998)055<0151:IOSANE>2.0.CO;2.

Di Girolamo, P., M. Cacciani, D. Summa, A. Scoccione, B. De Rosa, A. Behrendt, and V. Wulfmeyer, 2017: Characterisation of boundary layer turbulent processes by the Raman lidar BASIL in the frame of HD(CP)^2 Observational Prototype Experiment. *Atmos. Chem. Phys.*, **17**, 745–767, https://doi.org/10.5194/acp-17-745-2017.

Dirmeyer, P. A., and S. Halder, 2017: Application of the land–atmosphere coupling paradigm to the operational Coupled Forecast System (CFSv2). *J. Hydrometeor.*, **18**, 85–108, https://doi.org/10.1175/JHM-D-16-0064.1.

——, and Coauthors, 2012: Evidence for enhanced land–atmosphere feedback in a warming climate. *J. Hydrometeor.*, **13**, 981–995, https://doi.org/10.1175/JHM-D-11-0104.1.

Ducrocq, V., D. Ricard, J. P. Lafore, and F. Orain, 2002: Storm-scale numerical rainfall prediction for five precipitating events over France: On the importance of the initial humidity field. *Wea. Forecasting*, **17**, 1236–1256, https://doi.org/10.1175/1520-0434(2002)017<1236:SSNRPF>2.0.CO;2.

Ek, M. B., and A. A. M. Holtslag, 2004: Influence of soil moisture on boundary layer cloud development. *J. Hydrometeor.*, **5**, 86–99, https://doi.org/10.1175/1525-7541(2004)005<0086:IOSMOB>2.0.CO;2.

Ferguson, C. R., and E. F. Wood, 2011: Observed land–atmosphere coupling from satellite remote sensing and reanalysis. *J. Hydrometeor.*, **12**, 1221–1254, https://doi.org/10.1175/2011JHM1380.1.

Ferrare, R. A., and Coauthors, 2006: Evaluation of daytime measurements of aerosols and water vapor made by an operational Raman lidar over the southern Great Plains. *J. Geophys. Res.*, **111**, D05S08, https://doi.org/10.1029/2005JD005836.

Findell, K. L., and E. A. B. Eltahir, 2003a: Atmospheric controls on soil moisture–boundary layer interactions. Part I: Framework development. *J. Hydrometeor.*, **4**, 552–569, https://doi.org/10.1175/1525-7541(2003)004<0552:ACOSML>2.0.CO;2.

——, and ——, 2003b: Atmospheric controls on soil moisture–boundary layer interactions. Part II: Feedbacks within the continental United States. *J. Hydrometeor.*, **4**, 570–583, https://doi.org

/10.1175/1525-7541(2003)004<0570:ACOSML>2.0.CO;2.

Froidevaux, M., and Coauthors, 2013: A Raman lidar to measure water vapor in the atmospheric boundary layer. *Adv. Water Resour.*, **51**, 345–356, https://doi.org/10.1016/j.advwatres.2012.04.008.

Gentine, P., A. A. M. Holtslag, F. D'Andrea, and M. Ek, 2013: Surface and atmospheric controls on the onset of moist convection over land. *J. Hydrometeor.*, **14**, 1443–1462, https://doi.org/10.1175/JHM-D-12-0137.1.

Giez, A., G. Ehret, R. L. Schwiesow, K. J. Davis, and D. H. Lenschow, 1999: Water vapor flux measurements from ground-based vertically pointed water vapor differential absorption and Doppler lidars. *J. Atmos. Oceanic Technol.*, **16**, 237–250, https://doi.org/10.1175/1520-0426(1999)016<0237:WVFMFG>2.0.CO;2.

Goldsmith, J. E. M., F. H. Blair, S. E. Bisson, and D. D. Turner, 1998: Turn-key Raman lidar for profiling atmospheric water vapor, clouds, and aerosols. *Appl. Opt.*, **37**, 4979–4990, https://doi.org/10.1364/AO.37.004979.

Goutorbe, J.-P., and Coauthors, 1994: HAPEX-Sahel: A large-scale study of land-atmosphere interactions in the semi-arid tropics. *Ann. Geophys.*, **12**, 53–64, https://doi.org/10.1007/s00585-994-0053-0.

Grisogono, B., 2010: Generalizing 'z-less' mixing length for stable boundary layers. *Quart. J. Roy. Meteor. Soc.*, **136**, 213–221, https://doi.org/10.1002/qj.529.

Guillod, B. P., B. Orlowsky, D. G. Miralles, A. J. Teuling, and S. I. Seneviratne, 2015: Reconciling spatial and temporal soil moisture effects on afternoon rainfall. *Nat. Commun.*, **6**, 6443, https://doi.org/10.1038/ncomms7443.

Guo, Z., and Coauthors, 2006: GLACE: The Global Land–Atmosphere Coupling Experiment. Part II: Analysis. *J. Hydrol.*, **7**, 611–625, https://doi.org/10.1175/JHM511.1.

Gustafson, W. I., A. M. Vogelmann, X. Cheng, S. Endo, B. Krishna, Z. Li, T. Toto, and H. Xiao, 2017a: Description of the LASSO Alpha 1 Release. Robert Stafford, Ed., ARM Research Facility DOE/SC-ARM-TR-194, https://doi.org/10.2172/1373564.

——, ——, ——, ——, ——, ——, ——, and ——, 2017b: Recommendations for Implementation of the LASSO Workflow. R. Stafford, Ed., DOE Atmospheric Radiation Measurement Climate Research Facility DOE/SC-ARM-17-031, 62 pp, https://doi.org/10.2172/1406259.

Hall, F. G., 1999: BOREAS in 1999: Experiment and science overview. *J. Geophys. Res.*, **104**, 27 627–27 639, https://doi.org/10.1029/1999JD901026.

Hammann, E., A. Behrendt, F. Le Mounier, and V. Wulfmeyer, 2015: Temperature profiling of the atmospheric boundary layer with rotational Raman lidar during the HD(CP)^2 Observational Prototype Experiment. *Atmos. Chem. Phys.*, **15**, 2867–2881, https://doi.org/10.5194/acp-15-2867-2015.

Han, J. M., M. L. Witek, J. Teixeira, R. Sun, H.-L. Pan, J. K. Fletcher, and C. S. Bretherton, 2016: Implementation in the NCEP GFS of a hybrid eddy-diffusivity mass-flux (EDMF) boundary layer parameterization with dissipative heating and modified stable boundary layer mixing. *Wea. Forecasting*, **31**, 341–352, https://doi.org/10.1175/WAF-D-15-0053.1.

Heinze, R., and Coauthors, 2017: Large-eddy simulations over Germany using ICON: A comprehensive evaluation. *Quart. J. Roy. Meteor. Soc.*, **143**, 69–100, https://doi.org/10.1002/qj.2947.

Heus, T., and Coauthors, 2010: Formulation of the Dutch Atmospheric Large-Eddy Simulation (DALES) and over-view of its applications. *Geosci. Model Dev.*, **3**, 415–444, https://doi.org/10.5194/gmd-3-415-2010.

Higgins, C. W., E. Pardyjak, M. Froidevaux, V. Simeonov, and M. B. Parlange, 2013: Measured and estimated water vapor advection in the atmospheric surface layer. *J. Hydrometeor.*, **14**, 1966–1972, https://doi.org/10.1175/JHM-D-12-0166.1.

Hogan, R. J., A. L. M. Grant, A. J. Illingworth, G. N. Pearson, and E. J. O'Connor, 2009: Vertical velocity variance and skewness in clear and cloud-topped boundary layers as revealed by Doppler lidar. *Quart. J. Roy. Meteor. Soc.*, **135**, 635–643, https://doi.org/10.1002/qj.413.

Hohenegger, C., P. Brockhaus, C. S. Bretherton, and C. Schär, 2009: The soil moisture–precipitation feedback in simulations with explicit and parameterized convection. *J. Climate*, **22**, 5003–5020, https://doi.org/10.1175/2009JCLI2604.1.

Holtslag, A. A. M., and B. A. Boville, 1993: Local versus nonlocal boundary-layer diffusion in a global climate model. *J. Climate*, **6**, 1825–1842, https://doi.org/10.1175/1520-0442(1993)006<1825:LVNBLD>2.0.CO;2.

Honnert, R., V. Masson, and F. Couvreux, 2011: A diagnostic for evaluating the representation of turbulence in atmospheric models at the kilometric scale. *J. Atmos. Sci.*, **68**, 3112–3131, https://doi.org/10.1175/JAS-D-11-061.1.

——, F. Couvreux, V. Masson, and D. Lancz, 2016: Sampling the structure of convective turbulence and implications for grey-zone parametrizations. *Bound.-Layer Meteor.*, **160**, 133–156, https://doi.org/10.1007/s10546-016-0130-4.

Ito, J., H. Niino, M. Nakanishi, and C.-H. Moeng, 2015: An extension of Mellor–Yamada model to the terra incognita zone for dry convective mixed layers in the free convection regime. *Bound.-Layer Meteor.*, **157**, 23–43, https://doi.org/10.1007/s10546-015-0045-5.

Kiemle, C., and Coauthors, 2007: Latent heat flux profiles from collocated airborne water vapor and wind lidars during IHOP_2002. *J. Atmos. Oceanic Technol.*, **24**, 627–639, https://doi.org/10.1175/JTECH1997.1.

Klein, P., and Coauthors, 2015: LABLE: A multi-institutional, student-led, atmospheric boundary layer experiment. *Bull. Amer. Meteor. Soc.*, **96**, 1743–1764, https://doi.org/10.1175/BAMS-D-13-00267.1.

Knist, S., and Coauthors, 2016: Land-atmosphere coupling in EURO-CORDEX evaluation experiments. *J. Geophys. Res. Atmos.*, **122**, 79–103, https://doi.org/10.1002/2016JD025476.

Knuteson, R. O., and Coauthors, 2004a: Atmospheric Emitted Radiance Interferometer. Part I: Instrument design. *J. Atmos. Oceanic Technol.*, **21**, 1763–1776, https://doi.org/10.1175/JTECH-1662.1.

——, and Coauthors, 2004b: Atmospheric Emitted Radiance Interferometer. Part II: Instrument performance. *J. Atmos. Oceanic Technol.*, **21**, 1777–1789, https://doi.org/10.1175/JTECH-1663.1.

Koster, R. D., and Coauthors, 2006: GLACE: The Global Land–Atmosphere Coupling Experiment. Part I: Overview. *J. Hydrometeor.*, **7**, 590–610, https://doi.org/10.1175/JHM510.1.

Kotlarski, S., and Coauthors, 2014: Regional climate modeling on European scales: A joint standard evaluation of the EURO-CORDEX RCM ensemble. *Geosci. Model Dev.*, **7**, 1297–1333, https://doi.org/10.5194/gmdd-7-217-2014.

Lee, T. R., M. Buban, E. Dumas, and C. B. Baker, 2017: A new technique to estimate sensible heat fluxes around micrometeorological towers using small unmanned aircraft systems. *J. Atmos. Oceanic Technol.*, **34**, 2103–2112, https://doi.org/10.1175/JTECH-D-17-0065.1.

Lenderink, G., and E. Van Meijgaard, 2008: Increase in hourly precipitation extremes beyond expectations from temperature changes. *Nat. Geosci.*, **1**, 511–514, https://doi.org/10.1038/ngeo262.

Lenschow, D. H., J. Mann, and L. Kristensen, 1994: How long is long enough when measuring fluxes and other turbulence statistics? *J. Atmos. Oceanic Technol.*, **11**, 661–673, https://doi.org/10.1175/1520-0426(1994)011<0661:HLILEW>2.0.CO;2.

——, V. Wulfmeyer, and C. Senff, 2000: Measuring second-through fourth-order moments in noisy data. *J. Atmos. Oceanic Technol.*, **17**, 1330–1347, https://doi.org/10.1175/1520-0426(2000)017<1330:MSTFOM>2.0.CO;2.

——, M. Lothon, S. D. Mayor, P. P. Sullivan, and G. Canut, 2012: A comparison of higher-order vertical velocity moments in the convective boundary layer from lidar with in situ measurements and large-eddy simulation. *Bound.-Layer Meteor.*, **143**, 107–123, https://doi.org/10.1007/s10546-011-9615-3.

Linné, H., B. Hennemuth, J. Bösenberg, and K. Ertel, 2007: Water vapour flux profiles in the convective boundary layer. *Theor. Appl. Climatol.*, **87**, 201–211, https://doi.org/10.1007/s00704-005-0191-7.

Liu, Y., and Coauthors, 2011: Simultaneous nested modeling from the synoptic scale to the LES scale for wind energy applications. *J. Wind Eng. Ind. Aerodyn.*, **99**, 308–319, https://doi.org/10.1016/j.jweia.2011.01.013.

Long, C. N., J. H. Mather, and T. P. Ackerman, 2016: The ARM tropical western Pacific (TWP) sites. *The Atmospheric Radiation Measurement Program: The First 20 Years*, *Meteor. Monogr.*, No. 57, Amer. Meteor. Soc., 7.1–7.14, https://doi.org/10.1175/AMSMONOGRAPHS-D-15-0024.1.

Lorenz, R., and Coauthors, 2016: Influence of land–atmosphere feedbacks on temperature extremes in the GLACE-CMIP5 ensemble. *J. Geophys. Res. Atmos.*, **121**, 607–623, https://doi.org/10.1002/2015JD024053.

Lothon, M., and Coauthors, 2014: The BLLAST field experiment: Boundary-Layer Late Afternoon and Sunset Turbulence. *Atmos. Chem. Phys.*, **14**, 10931–10960, https://doi.org/10.5194/acp-14-10931-2014.

Lundquist, J. K., and Coauthors, 2017: Assessing state-of-the-art capabilities for probing the atmospheric boundary layer: The XPIA field campaign. *Bull. Amer. Meteor. Soc.*, **98**, 289–314, https://doi.org/10.1175/BAMS-D-15-00151.1.

Macke, A., and Coauthors, 2017: The HD(CP)^2 Observational Prototype Experiment (HOPE)—An overview. *Atmos. Chem. Phys.*, **17**, 4887–4914, https://doi.org/10.5194/acp-17-4887-2017.

Mahmood, R., and Coauthors, 2014: Land cover changes and their biogeophysical effects on climate. *Int. J. Climatol.*, **34**, 929–953, https://doi.org/10.1002/joc.3736.

Maronga, B., and Coauthors, 2015: The Parallelized Large-Eddy Simulation Model (PALM) version 4.0 for atmospheric and oceanic flows: Model formulation, recent developments, and future perspectives. *Geosci. Model Dev.*, **8**, 2515–2551, https://doi.org/10.5194/gmd-8-2515-2015.

Massey, J. D., W. J. Steenburgh, J. C. Knievel, and W. Y. Y. Cheng, 2016: Regional soil moisture biases and their

influence on WRF Model temperature forecasts over the Intermountain West. *Wea. Forecasting*, **31**, 197–216, https://doi.org/10.1175/WAF-D-15-0073.1.

McNicholas, C., and D. D. Turner, 2014: Characterizing the convective boundary layer turbulence with a High Spectral Resolution Lidar. *J. Geophys. Res. Atmos.*, **119**, 12 910–12 927, https://doi.org/10.1002/2014JD021867.

Mellor, G. L., and T. Yamada, 1982: Development of a turbulence closure model for geophysical fluid problems. *Rev. Geophys. Space Phys.*, **20**, 851–875, https://doi.org/10.1029/RG020i004p00851.

Michael, P., 1994: Estimating advective tendencies from field measurements. *Mon. Wea. Rev.*, **122**, 2202–2209.

Milovac, J., K. Warrach-Sagi, A. Behrendt, F. Späth, J. Ingwersen, and V. Wulfmeyer, 2016: Investigation of PBL schemes combining the WRF model simulations with scanning water vapor differential absorption lidar measurements. *J. Geophys. Res. Atmos.*, **121**, 624–649, https://doi.org/10.1002/2015JB012593.

Morrison, T. J., M. Calaf, H. J. S. Fernando, T. A. Price, and E. R. Pardyjak, 2017: A methodology for computing spatially and temporally varying surface sensible heat flux from thermal imagery. *Quart. J. Roy. Meteor. Soc.*, **143**, 2616–2624, https://doi.org/10.1002/qj.3112.

Muppa, S. K., A. Behrendt, F. Späth, V. Wulfmeyer, S. Metzendorf, and A. Riede, 2016: Turbulent humidity fluctuations in the convective boundary layer: Case studies using water vapour differential absorption lidar measurements. *Bound.-Layer Meteor.*, **158**, 43–66, https://doi.org/10.1007/s10546-015-0078-9.

Neggers, R. A. J., A. P. Siebesma, and T. Heus, 2012: Continuous single-column model evaluation at a permanent meteorological supersite. *Bull. Amer. Meteor. Soc.*, **93**, 1389–1400, https://doi.org/10.1175/BAMS-D-11-00162.1.

Newsom, R. K., D. D. Turner, B. Mielke, M. Clayton, R. Ferrare, and C. Sivaraman, 2009: The use of simultaneous analog and photon counting detection for Raman lidar. *Appl. Opt.*, **48**, 3903–3914, https://doi.org/10.1364/AO.48.003903.

——, ——, and J. E. M. Goldsmith, 2013: Long-term evaluation of temperature profiles measured by an operational Raman lidar. *J. Atmos. Oceanic Technol.*, **30**, 1616–1634, https://doi.org/10.1175/JTECHD-12-00138.1.

Osman, M. K., D. D. Turner, T. Heus, and R. K. Newsom, 2018: Characteristics of water vapor turbulence profiles in convective boundary layers during the dry and wet seasons over Darwin. *J. Geophys. Res.*, **123**, 4818–4836, https://doi.org/10.1029/2017JD028060.

Päschke, E., R. Leinweber, and V. Lehmann, 2015: An assessment of the performance of a 1.5 μm Doppler lidar for operational vertical wind profiling based on a 1-year period. *Atmos. Meas. Tech.*, **8**, 2251–2266, https://doi.org/10.5194/amt-8-2251-2015.

Pearson, G., Fa. Davies, and C. Collier, 2009: An analysis of the performance of the UFAM pulsed Doppler lidar for observing the boundary layer. *J. Atmos. Oceanic Technol.*, **26**, 240–250, https://doi.org/10.1175/2008JTECHA1128.1.

Pichugina, Y. L., and R. M. Banta, 2010: Stable boundary-layer depth from high-resolution measurements of the mean wind profile. *J. Appl. Meteor. Climatol.*, **49**, 20–35, https://doi.org/10.1175/2009JAMC2168.1.

Pleim, J. E., 2007: A combined local and nonlocal closure model for the atmospheric boundary layer. Part II: Application and evaluation in a mesoscale meteorological model. *J. Appl. Meteor. Climatol.*, **46**, 1383–1395, https://doi.org/10.1175/JAM2539.1.

Prein, A. F., and Coauthors, 2015: A review on regional convection-permitting climate modeling: Demonstrations, prospects, and challenges. *Rev. Geophys.*, **53**, 323–361, https://doi.org/10.1002/2014RG000475.

Radlach, M., A. Behrendt, and V. Wulfmeyer, 2008: Scanning rotational Raman lidar at 355 nm for the measurement of tropospheric temperature fields. *Atmos. Chem. Phys.*, **8**, 159–169, https://doi.org/10.5194/acp-8-159-2008.

Roundy, J. K., C. R. Ferguson, and E. F. Wood, 2013: Temporal variability of land–atmosphere coupling and its implications for drought over the southeast United States. *J. Hydrometeor.*, **14**, 622–635, https://doi.org/10.1175/JHM-D-12-090.1.

Sakradzija, M., A. Seifert, and A. Dipankar, 2016: A stochastic scale-aware parameterization of shallow cumulus convection across the convective gray zone. *J. Adv. Model. Earth Syst.*, **8**, 786–812, https://doi.org/10.1002/2016MS000634.

Santanello, J. A., C. Peters-Lidard, S. Kumar, C. Alonge, and W.-K. Tao, 2009: A modeling and observational framework for diagnosing local land–atmosphere coupling on diurnal time scales. *J. Hydrometeor.*, **10**, 577–599, https://doi.org/10.1175/2009JHM1066.1.

——, ——, and —, 2011: Diagnosing the sensitivity of local land–atmosphere coupling via the soil moisture–boundary layer interaction. *J. Hydrometeor.*, **12**, 766–786, https://doi.org/10.1175/JHM-D-10-05014.1.

——, ——, A. Kennedy, and S. Kumar, 2013: Diagnosing the nature of land–atmosphere coupling: A case study of dry/wet extremes in the U.S. southern Great Plains. *J. Hydrometeor.*, **14**, 3–24, https://doi.org/10.1175/JHM-D-12-023.1.

——, and Coauthors, 2018: Land–atmosphere interactions: The LoCo perspective. *Bull. Amer. Meteor. Soc.*, https://doi.org/10.1175/BAMS-D-17-0001.1, in press.

Sathe, A., J. Mann, N. Vasiljevic, and G. Lea, 2015: A six-beam method to measure turbulence statistics using ground-based wind lidars. *Atmos. Meas. Tech.*, **8**, 729–740, https://doi.org/10.5194/amt-8-729-2015.

Schwitalla, T., H.-S. Bauer, V. Wulfmeyer, and K. Warrach-Sagi, 2017: Continuous high-resolution mid-latitude belt simulations for July-August 2013 with WRF. *Geosci. Model Dev.*, **10**, 2031–2055, https://doi.org/10.5194/gmd-10-2031-2017.

Sellers, P. J., F. G. Hall, G. Asrar, D. E. Strebel, and R. E. Murphy, 1988: The First ISLSCP Field Experiment (FIFE). *Bull. Amer. Meteor. Soc.*, **69**, 22–27, https://doi.org/10.1175/1520-0477(1988)069<0022:TFIFE>2.0.CO;2.

Seneviratne, S. I., D. Lüthi, M. Litschi, and C. Schär, 2006: Land–atmosphere coupling and climate change in Europe. *Nature*, **443**, 205–209, https://doi.org/10.1038/nature05095.

——, T. Corti, E. L. Davin, M. Hirschi, E. B. Jaeger, I. Lehner, B. Orlowski, and A. J. Teuling, 2010: Investigating soil moisture–climate interactions in a changing climate: A review. *Earth-Sci. Rev.*, **99**, 125–161, https://doi.org/10.1016/j.earscirev.2010.02.004.

Senff, C., J. Bösenberg, and G. Peters, 1994: Measurement of water vapor flux profiles in the convective boundary layer with lidar and radar–RASS. *J. Atmos. Oceanic Technol.*, **11**, 85–93, https://doi.org/10.1175/1520-0426(1994)011<0085:MOWVFP>2.0.CO;2.

Sherwood, S. C., R. Roca, T. M. Weckwerth, and N. G. Andronova, 2010: Tropospheric water vapor, convection, and climate. *Rev. Geophys.*, **48**, RG2001, https://doi.org/10.1029/2009RG000301.

Shin, H. H., and S. Y. Hong, 2011: Intercomparison of planetary boundary-layer parametrizations in the WRF model for a single day from CASES-99. *Bound.-Layer Meteor.*, **139**, 261–281, https://doi.org/10.1007/s10546-010-9583-z.

——, and ——, 2015: Representation of the subgrid-scale turbulent transport in convective boundary layers at gray-zone resolutions. *Mon. Wea. Rev.*, **143**, 250–271, https://doi.org/10.1175/MWR-D-14-00116.1.

Siebesma, A. P., and J. Teixeira, 2000: An advection–diffusion scheme for the convective boundary layer, description and 1D results. *Proc. 14th Symp. on Boundary Layers and Turbulence*, Aspen, CO, Amer. Meteor. Soc., 133–136.

——, P. M. M. Soares, and J. Teixeira, 2007: A combined eddy-diffusivity mass-flux approach for the convective boundary layer. *J. Atmos. Sci.*, **64**, 1230–1248, https://doi.org/10.1175/JAS3888.1.

Sisterson, D. L, R. A. Peppler, T. S. Cress, P. J. Lamb, and D. D. Turner, 2016: The ARM Southern Great Plains (SGP) site. *The Atmospheric Radiation Measurement Program: The First 20 Years*, *Meteor. Monogr.*, No. 57, Amer. Meteor. Soc., 6.1–6.14, https://doi.org/10.1175/AMSMONOGRAPHS-D-16-0004.1.

Späth, F., A. Behrendt, S. K. Muppa, S. Metzendorf, A. Riede, and V. Wulfmeyer, 2016: 3-D water vapor field in the atmospheric boundary layer observed with scanning differential absorption lidar. *Atmos. Meas. Tech.*, **9**, 1701–1720, https://doi.org/10.5194/amt-9-1701-2016.

Spuler, S. M., K. S. Repasky, B. Morley, D. Moen, M. Hayman, and A. R. Nehrir, 2015: Field-deployable diode-laser-based differential absorption lidar (DIAL) for profiling water vapor. *Atmos. Meas. Tech.*, **8**, 1073–1087, https://doi.org/10.5194/amt-8-1073-2015.

Stéfanon, M., P. Drobinski, F. D'Andrea, C. Lebeaupin-Brossier, and S. Bastin, 2014: Soil moisture-temperature feedbacks at meso-scale during heat waves over western Europe. *Climate Dyn.*, **42**, 1309–1324, https://doi.org/10.1007/s00382-013-1794-9.

Sühring, M., and S. Raasch, 2013: Heterogeneity-induced heat-flux patterns in the convective boundary layer: Can they be detected from observations and is there a blending height? A large-eddy simulation study for the LITFASS-2003 experiment. *Bound.-Layer Meteor.*, **148**, 309–331, https://doi.org/10.1007/s10546-013-9822-1.

Tastula, E. M., M. A. LeMone, J. Dudhia, and B. Galperin, 2016: The impact of the QNSE-EDMF scheme and its modifications on boundary layer parameterization in WRF: Modelling of CASES-97. *Quart. J. Roy. Meteor. Soc.*, **142**, 1182–1195, https://doi.org/10.1002/qj.2723.

Tawfik, A. B., P. A. Dirmeyer, and J. A. Santanello, 2015: The heated condensation framework. Part II: Climatological behavior of convective initiation and land–atmosphere coupling over the conterminous United States. *J. Hydrometeor.*, **16**, 1946–1961, https://doi.org/10.1175/JHM-D-14-0118.1.

Taylor, C. M., R. A. M. de Jeu, F. Guichard, P. P. Harris, and W. A. Dorigo, 2012: Afternoon rain more likely over dry soils. *Nature*, **489**, 423–426, https://doi.org/10.1038/nature11377.

Teixeira, J., and S. Cheinet, 2004: A simple mixing length formulation for the eddy-diffusivity parameterization of dry convection. *Bound.-Layer Meteor.*, **110**, 435–453, https://doi.org/10.1023/B:BOUN.0000007230.96303.0d.

Turner, D. D., and J. E. M. Goldsmith, 1999: Twenty-four-hour Raman lidar water vapor measurements during the Atmospheric Radiation Measurement Program's 1996 and 1997 water vapor intensive observation periods. *J. Atmos. Oceanic Technol.*, **16**, 1062–1076, https://doi.org/10.1175/1520-0426(1999)016<1062:TFHRLW>2.0.CO;2.

——, R. A. Ferrare, L. A. Heilman Brasseur, W. F. Feltz, and T. P. Tooman, 2002: Automated retrievals of water vapor and aerosol profiles over Oklahoma from an operational Raman lidar. *J. Atmos. Oceanic Technol.*, **19**, 37–50, https://doi.org/10.1175/1520-0426(2002)019<0037:AROWVA>2.0.CO;2.

——, ——, V. Wulfmeyer, and A. J. Scarino, 2014a: Aircraft evaluation of ground-based Raman lidar water vapor turbulence profiles in convective mixed layers. *J. Atmos. Oceanic Technol.*, **31**, 1078–1088, https://doi.org/10.1175/JTECH-D-13-00075.1.

——, V. Wulfmeyer, L. K. Berg, and J. H. Schween, 2014b: Water vapor turbulence profiles in stationary continental convective mixed layers. *J. Geophys. Res. Atmos.*, **119**, 11 165–11 165, https://doi.org/10.1002/2014JD022202.

——, J. E. M. Goldsmith, and R. A. Ferrare, 2016: Development and applications of the ARM Raman lidar. *The Atmospheric Radiation Measurement Program: The First 20 Years*, *Meteor. Monogr.*, No. 57, Amer. Meteor. Soc., 18.1–18.15, https://doi.org/10.1175/AMSMONOGRAPHS-D-15-0026.1.

——, V. Wulfmeyer, A. Behrendt, T. A. Bonin, A. Choukulkar, R. K. Newsom, W. A. Brewer, and D. R. Cook, 2018: Response of the land-atmosphere system over north-central Oklahoma during the 2017 eclipse. *Geophys. Res. Lett.*, **45**, 1668–1675, https://doi.org/10.1002/2017GL076908.

Van de Boer, A., A. F. Moene, A. Graf, D. Schüttemeyer, and C. Simmer, 2014: Detection of entrainment influences on surface-layer measurements and extension of Monin–Obukhov similarity theory. *Bound.-Layer Meteor.*, **152**, 19–44, https://doi.org/10.1007/s10546-014-9920-8.

Van den Hurk, B., M. Best, P. Dirmeyer, A. Pitman, J. Polcher, and J. Santanello, 2011: Acceleration of land surface model development over a decade of GLASS. *Bull. Amer. Meteor. Soc.*, **92**, 1593–1600, https://doi.org/10.1175/BAMS-D-11-00007.1.

Vautard, R., and Coauthors, 2013: The simulation of European heat waves from an ensemble of regional climate models within the EURO-CORDEX project. *Climate Dyn.*, **41**, 2555–2575, https://doi.org/10.1007/s00382-013-1714-z.

Wagner, G., V. Wulfmeyer, F. Späth, A. Behrendt, and M. Schiller, 2013: Performance and specifications of a pulsed high-power single-frequency Ti:sapphire laser for water-vapor differential absorption lidar. *Appl. Opt.*, **52**, 2454–2469, https://doi.org/10.1364/AO.52.002454.

Warrach-Sagi, K., T. Schwitalla, V. Wulfmeyer, and H.-S. Bauer, 2013: Evaluation of a climate simulation based on the WRF–NOAH model system: Precipitation in Germany. *Climate Dyn.*, **41**, 755–774, https://doi.org/10.1007/s00382-013-1727-7.

Weckwerth, T. M., and Coauthors, 2004: An overview of the International H_2O Project (IHOP_2002) and some preliminary highlights. *Bull. Amer. Meteor. Soc.*, **85**, 253–277, https://doi.org/10.1175/BAMS-85-2-253.

——, K. Weber, D. D. Turner, and S. M. Spuler, 2016: Validation of a new water vapor micropulse differential absorption lidar (DIAL). *J. Atmos. Oceanic Technol.*, **33**, 2353–2372, https://doi.org/10.1175/JTECH-D-16-0119.1.

Weng, W., and P. Taylor, 2003: On modelling the one-dimensional atmospheric boundary layer. *Bound.-Layer Meteor.*, **107**, 371–400, https://doi.org/10.1023/A:1022126511654.

Whiteman, D., 2003a: Examination of the traditional Raman lidar technique. I. Evaluating the temperature-dependent lidar equations. *Appl. Opt.*, **42**, 2571–2592, https://doi.org/10.1364/AO.42.002571.

——, 2003b: Examination of the traditional Raman lidar technique. II. Evaluating the ratios for water vapor and aerosols. *Appl. Opt.*, **42**, 2593–2608, https://doi.org/10.1364/AO.42.002593.

Wizemann, H.-D., J. Ingwersen, P. Högy, K. Warrach-Sagi, T. Streck, and V. Wulfmeyer, 2015: Three year observations of water vapor and energy fluxes over agricultural crops in two regional climates of southwest Germany. *Meteor. Z.*, **24**, 39–59, https://doi.org/10.1127/metz/2014/0618.

Wolf, B., and Coauthors, 2017: The SCALEX campaign: Scale-crossing land-surface and boundary layer processes in the TERENO-prealpine observatory. *Bull. Amer. Meteor. Soc.*, **98**, 1217–1234, https://doi.org/10.1175/BAMS-D-15-00277.1.

Wulfmeyer, V., 1999a: Investigation of turbulent processes in the lower troposphere with water vapor DIAL and radar–RASS. *J. Atmos. Sci.*, **56**, 1055–1076, https://doi.org/10.1175/1520-0469(1999)056<1055:IOTPIT>2.0.CO;2.

——, 1999b: Investigations of humidity skewness and variance profiles in the convective boundary layer and comparison of the latter with large eddy simulation results. *J. Atmos. Sci.*, **56**, 1077–1087, https://doi.org/10.1175/1520-0469(1999)056<1077:IOHSAV>2.0.CO;2.

——, and T. Janjić, 2005: 24-h observations of the marine boundary layer using ship-borne NOAA high-resolution Doppler lidar. *J. Appl. Meteor.*, **44**, 1723–1744, https://doi.org/10.1175/JAM2296.1.

——, D. D. Turner, S. Pal, and E. Wagner, 2010: Can water vapour Raman lidar resolve profiles of turbulent variables in the convective boundary layer? *Bound.-Layer Meteor.*, **136**, 253–284, https://doi.org/10.1007/s10546-010-9494-z.

——, and Coauthors, 2011: The Convective and Orographically Induced Precipitation Study (COPS): The Scientific Strategy, the Field Phase, and First Highlights. *Quart. J. Roy. Meteor. Soc.,* **137,** 3–30, https://doi.org/10.1002/qj.752.

——, and Coauthors, 2015a: A review of the remote sensing of lower-tropospheric thermodynamic profiles and its indispensable role for the understanding and the simulation of water and energy cycles. *Rev. Geophys.*, **53**, 819–895, https://doi.org/10.1002/2014RG000476.

——, and Coauthors, 2015b: New concepts for studying land-surface-atmosphere feedback based on a new lidar synergy and gray zone simulations. Geophysical Research Abstracts, Vol. 17, Abstract 5054, http://meetingorganizer.copernicus.org/EGU2015/EGU2015-5054.pdf.

——, S. K. Muppa, A. Behrendt, S. M. E. Hammann, F. Späth, Z. Sorbjan, D. D. Turner, and R. M. Hardesty, 2016: Determination of convective boundary layer entrainment fluxes, dissipation rates, and the molecular destruction of variances: Theoretical description and a strategy for its confirmation with a novel lidar system synergy. *J. Atmos. Sci.,* **73,** 667–692, https://doi.org/10.1175/JAS-D-14-0392.1.

Wyngaard, J. C., 2004: Toward numerical modeling in the terra incognita. *J. Atmos. Sci.*, **61**, 1816–1826, https://doi.org/10.1175/1520-0469(2004)061<1816:TNMITT>2.0.CO;2.

Zolina, O. C., C. Simmer, K. Belyaev, K. Sergey, S. Gulev, and A. N. D. P. Koltermann, 2013: Changes in the duration of European wet and dry spells during the last 60 years. *J. Climate*, **26**, 2022–2047, https://doi.org/10.1175/JCLI-D-11-00498.1.

Radar and Atmospheric Science: A Collection of Essays in Honor of David Atlas

Edited by Roger M. Wakimoto and Ramesh Srivastava

This monograph pays tribute to one of the leading scientists in meteorology, Dr. David Atlas. In addition to profiling the life and work of the acknowledged "Father of Radar Meteorology," this collection highlights many of the unique contributions he made to the understanding of the forcing and organization of convective systems, observation and modeling of atmospheric turbulence and waves, and cloud microphysical properties, among many other topics. It is hoped that this text will inspire the next generation of radar meteorologists, provide an excellent resource for scientists and educators, and serve as a historical record of the gathering of scholarly contributions honoring one of the most important meteorologists of our time.

Radar and Atmospheric Science: A Collection of Essays in Honor of David Atlas

Aug 2003. Meteorological Monograph Series, Vol. 30, No. 52; 270 pp, hardbound; ISBN 1-878220-57-8; AMS code MM52.

Price $80.00 member

To place an order point your Web browser to www.ametsoc.org/amsbookstore

AMS BOOKS

RESEARCH ◆ APPLICATIONS ◆ HISTORY